RSC Advances

PAPER

View Article Online
View Journal | View Issue

Cite this: *RSC Adv.*, 2026, **16**, 16424

Synergistic elimination of antibiotic resistance genes and tetracycline antibiotics in wastewater *via* a Z-scheme Bi_2WO_6/g-C_3N_4 heterojunction: degradation pathways and mechanism

Yuankun Liu, *[a] Gangyi Sun,[a] Yuanqi Cao,[a] Xing Li,[a] Zhangya Li[a] and Zhonglin Chen*[b]

Antibiotics and antibiotic resistance genes (ARGs) pose a serious threat to ecosystems and human health. Photocatalytic technology is a hotspot in the pollutant purification. A novel Z-scheme Bi_2WO_6/g-C_3N_4 heterojunction was successfully synthesized and demonstrated exceptional photocatalytic efficacy illuminated by visible light, effectively degrading three different tetracycline antibiotics, and it more over demonstrated impressive effectiveness in ARGs from secondary effluent. The removal rates for *16S rRNA*, *intI1*, *tetA*, *tetC*, *sulI* and *sulII* were notably high, with reductions of 3.04 log, 2.88 log, 3.15 log, 3.68 log, 2.71 log and 2.64 log, respectively. And the removal of DOC in secondary effluents is of great significance for reducing ARGs. h^+ and $^{\bullet}O_2^-$ were validated to be primary active substances for removing TCs and ARGs in the process. Active species can directly destroy the structure of microbial cells and cause DNA damage. *16S rRNA*, *intI1* and DOC were significant positive correlations with ARGs. The migration pathway of photogenerated carriers on the surface of Z-scheme heterojunction and photocatalytic degradation mechanism for removing TCs and ARGs were also studied. Finally, degradation byproducts, process and pathways of TC were investigated. This study presents a novel strategy for efficiently removing TCs and ARGs, thereby mitigating the spread of them.

Received 9th December 2025
Accepted 13th March 2026

DOI: 10.1039/d5ra09524g

rsc.li/rsc-advances

1. Introduction

As industrialization and population continue to develop, the issues of energy crisis and environmental pollution have drawn widespread attention worldwide.[1–4] Since the introduction of penicillin in 1928, the global use of antibiotics has increased year by year, and they are widely used in fields such as daily health care, disease treatment and aquaculture.[5,6] Tetracyclines (TCs) are a class of broad-spectrum antibiotics primarily used to treat various infections caused by bacteria. Their versatility extends to tackling intracellular pathogens such as Chlamydia, Rickettsia, and Mycoplasma, solidifying their reputation as a reliable choice for addressing a range of bacterial infections.[7,8] However, due to incomplete absorption by humans and animals, more than 50% of these antibiotics are excreted into the environment as metabolic by-products.[9] Because of this, water environments have higher concentrations of residual antibiotics,[10] which encourages the growth of bacteria resistant to antibiotic resistant bacteria (ARB) and the dissemination of genes that cause antibiotic resistance genes (ARGs).[11,12] ARGs are widespread in the environment and are replicable, transmissible and environmentally persistent. They can enter the bodies of animals and humans through multiple pathways, augmenting bacterial resistance and undermining the effectiveness of antibiotics in disease control and clinical treatment.[13,14] Currently, ARGs have become a major challenge in the field of global public health, imposing significant risks of gene pollution on water, agricultural and human living environments, thereby causing long-term and irreversible harm to ecosystem safety.[15,16] Consequently, it is crucial to effectively remove the residues of TCs and ARGs for preserving the ecological environment and ensuring human health.

Recent studies have revealed that, the advancement of photocatalytic technology has presented a novel and cost-effective approach to the efficient treatment of water pollution.[17,18] Photocatalysis transforms solar energy directly into chemical energy, providing benefits like straightforward operation, thorough degradation of pollutants and absence of secondary pollution.[19–22] Therefore, it has been widely used in the treatment of difficult-to-degrade pollutants. g-C_3N_4, a promising semiconductor photocatalytic material, possesses a bandgap of approximately 2.7 eV. There are many advantages in wastewater treatment, such as easy preparation, rapid visible light response

[a]*College of Architecture and Civil Engineering, Beijing University of Technology, Beijing 100124, P. R. China. E-mail: liuyuankun@bjut.edu.cn*

[b]*State Key Laboratory of Urban-rural Water Resources and Environment, Harbin Institute of Technology, Harbin 150090, P. R. China. E-mail: zhonglinchen@hit.edu.cn*

non-toxic and non-polluting, which exhibit it as an environmentally friendly photocatalytic material.[23–26] However, bulk g-C_3N_4 is characterized by a restricted surface area and a low potential at the valence band level.[27,28]

To overcome these shortcomings, researchers frequently enhance its photocatalytic activity through modification.[29–32] For example, Cadan *et al.*[33] synthesized g-C_3N_4/WO_3 composites using an ultrasonic-assisted method to improve pollutant removal rates. Chen *et al.*[34] prepared NiSe/g-C_3N_4 photocatalyst by hydrothermal method, which showed excellent H_2 production and outstanding degradation efficiency towards methyl orange and tetracycline. In addition, Song *et al.*[35] uniformly dispersed silver nanoparticles on g-C_3N_4 through photoreduction to prepare Ag/g-C_3N_4 composites, which significantly improved the degradation performance of sulfamethoxazole. Therefore, altering g-C_3N_4 is vital for enhancing its photocatalytic performance.

Bi_2WO_6, an aurivillius oxide, has a 2.7–2.85 eV band gap and shows excellent photocatalytic degradation ability under visible light.[36–39] Bi_2WO_6 forms an orthorhombic crystal lattice, featuring alternating $(Bi_2O_2)_n^{2n+}$ sheets and perovskite-like $(WO_4)_n^{2n-}$ octahedral layers. Bi_2WO_6 and g-C_3N_4 share a remarkably similar band structure, which facilitates the creation of a Bi_2WO_6/g-C_3N_4 heterojunction that demonstrates outstanding photocatalytic capabilities. For instance, Chen *et al.*[40] employed a single-step *in situ* hydrothermal approach to synthesize the Bi_2WO_6/g-C_3N_4 catalyst, later used for the photocatalytic breakdown of ammonium dinitramide (ADN). However, there was less research on the implementation of Bi_2WO_6/g-C_3N_4 to TCs and ARGs than the material preparation. Since conventional wastewater treatment technologies have limited capacity to remove refractory pollutants, it is crucial to understand the degradation performance and mechanism of Bi_2WO_6/g-C_3N_4 photocatalysis technology for TCs and ARGs.

A Z-scheme Bi_2WO_6/g-C_3N_4 heterojunction was successfully prepared using the hydrothermal method, with g-C_3N_4 serving as the carrier. Through optimizing the preparation conditions, composites with excellent photocatalytic oxidation performance were obtained. Various characterization approaches were applied to investigate the close connection between the structural properties of the materials and their photocatalytic performance, such as XPS, SEM, XRD, *etc.* The degradation efficiency of Bi_2WO_6/g-C_3N_4 was investigated for three types of TCs (TC, CTC, OTC) and ARGs to comprehensively evaluate their photocatalytic activity and applicability. In addition, photocatalytic experiments under diverse conditions verified the robust and reliable photocatalytic performance of Bi_2WO_6/g-C_3N_4. The photocatalytic performance of Bi_2WO_6/g-C_3N_4 in degrading TC and ARGs was thoroughly assessed. Key factors, such as the quantity of catalyst utilized, the concentration of TC, initial pH levels, the presence of HA, and various anions, were meticulously analyzed. Ultimately, the potential degradation routes for TC and the fundamental photocatalytic mechanisms associated with Bi_2WO_6/g-C_3N_4 were extensively investigated. This work delivers a cutting-edge solution for the effective removal of TCs and ARGs, reducing the dissemination risk of ARGs and offering promising prospects for broad application in the field of wastewater purification.

2. Materials and methods

2.1. Experimental materials

The main experimental materials are provided in Text S1. And the specific water quality indicators are listed in Table S1.

2.2. Preparation of catalysts

2.2.1. Synthesis of g-C_3N_4. The preparation of g-C_3N_4 was carried out in accordance with the procedures detailed in Text S2.

2.2.2. Synthesis of Bi_2WO_6/g-C_3N_4 composites. Composite materials of Bi_2WO_6/g-C_3N_4 were created using a hydrothermal approach. Initially, a designated quantity of $Bi(NO_3)_3 \cdot 5H_2O$ was dissolved in 5 mL of glacial acetic acid, after which 10 mL of deionized water was incorporated. This combination was then sonicated for half an hour, producing what is termed solution A. Meanwhile, $Na_2WO_4 \cdot 2H_2O$ and 50 mg of CTAB were dissolved in 25 mL of deionized water, followed by an additional 30 minutes of sonication, resulting in solution B. Finally, while stirring magnetically, solution B was gradually introduced to solution A, drop by drop. After thorough stirring, a certain quantity of g-C_3N_4 was added to achieve a 15% mass proportion of Bi_2WO_6 relative to g-C_3N_4. The solution's pH was carefully fine-tuned to 3 by adding precise amounts of NaOH and HCl. Once the desired acidity was achieved, the mixture was poured into a 200 mL PTFE-lined reactor and subjected to calcination at 160 °C for a solid 12 hours. After the reactor had cooled down to room temperature, the resulting sample underwent a thorough cleaning process: the sample was rinsed three times using deionized water and anhydrous ethanol, and then dried in a 60 °C oven for 10 hours. Additionally, pure Bi_2WO_6 was prepared employing an identical approach described above, but without the addition of g-C_3N_4 during the preparation.

The Bi_2WO_6/g-C_3N_4 mass ratio, precursor solution pH, and calcination temperature used above, which are the importance and key parameters in the synthesis of Bi_2WO_6/g-C_3N_4, have been carried out by the preliminary optimization experiments (Fig. S1 and Text S3).

2.3. Characterization

For detailed information on the main features, refer to Text S4.

2.4. Photocatalytic degradation experiments

The degradation of TCs at 25 °C was employed to assess the photocatalytic efficacy of Bi_2WO_6/g-C_3N_4 under visible light. The light source employs a 300 W xenon lamp (CEL-HXF300E7, CEULIGHT) equipped with a 420 nm optical filter. The mean light intensity, ascertained using an optical power density meter (NP2000, CEAULIGHT) was found to be 212 mW cm^{-2}. The distance from the reaction solution's surface to the light source was roughly 10 centimeters. In each experiment, 1.0 g per L Bi_2WO_6/g-C_3N_4 was included into the TCs solution (20 mg L^{-1}), and the mixture was agitated continuously for 30 minutes in the

absence of light to attain adsorption–desorption equilibrium. The photocatalytic process persisted for 140 minutes. At regular intervals, 5 mL of the suspension was extracted and subsequently filtered through a 0.45-μm filter to remove the produced catalysts. The UV-visible spectrophotometer (UV-1900) was employed to quantify the concentration of TC at 357 nm. The concentrations of CTC and OTC were assessed and quantified at 367 nm and 353 nm, respectively. All aforementioned studies were conducted thrice, and the mean values were regarded as the experimental outcomes.

The first-order kinetic model formula is as follows:[41]

$$-\ln\left(\frac{C_t}{C_0}\right) = kt \quad (1)$$

where C_0 (mg L^{-1}) refers to the pollutant's starting concentration once adsorption equilibrium is achieved, while C_t (mg L^{-1}) corresponds to the pollutant's concentration at different points in time throughout the photocatalytic process. k (min^{-1}) stands for the kinetic constant of the reaction, and t (min) denotes the total time the reaction has been underway.

The factors affecting photocatalytic degradation, such as catalyst amount, pollutant levels, pH, inorganic ions, and organic compounds, were assessed and examined.

2.5. Analytical methods

The transient photocurrent response as well as the electrochemical impedance of the samples were subjected to analysis and determination with the employment of an electrochemical workstation (P4000, Ametek) within a three-electrode system. The experimental setup consisted of an FTO glass working electrode layered with the sample material, alongside a platinum electrode serving as the counter electrode, and a saturated mercury electrode used as the reference electrode. The system employed a 0.5 M Na_2SO_4 solution as the electrolyte. A 300 W Xe lamp emitting visible light between 420 nm and 700 nm was utilized for the experiments. Room temperature was the condition under which all electrochemical tests were conducted. To ascertain the active species involved in the photocatalytic process, disodium ethylenediaminetetraacetate (EDTA-2Na), isopropyl alcohol (IPA), and TEMPOL were employed as scavengers for holes (h^+), hydroxyl radicals ($^{\bullet}OH$), and superoxide radicals ($^{\bullet}O_2^-$), respectively. The presence of reactive oxygen species (ROS) was confirmed using electron paramagnetic resonance (EPR) (JES-FA200, JEOL). The degradation intermediates of TC were determined by HPLC/MS (Agilent 6460 Triple Quad LC/MS) equipped with a C18 column (Agilent Zorbax Eclipse Plus, 2.1 mm × 50 mm, 1.8 μm). The mobile phase comprised a 5 : 95 blend of ultrapure water (0.1% formic acid) and acetonitrile, with a flow rate of 0.20 mL min^{-1} and an injection volume of 10.00 μL. Both positive electrospray ionization (ESI+) and negative electrospray ionization (ESI−) modes were utilized for the study.

2.6. Photocatalytic inactivation of ARGs

In this study, the representative water quality was the secondary-treated effluent from a wastewater treatment plant. Considering the increased prevalence of tetracycline resistance genes (*tetA*, *tetC*) and sulfonamide resistance genes (*sulI*, *sulII*) in the secondary effluent, these genes were selected as the target genes to investigate the removal efficiency of Bi_2WO_6/g-C_3N_4 photocatalytic technology for ARGs. In the experiment, a specific quantity of catalyst was mixed into 500 mL of secondary effluent and agitated for 140 minutes under visible light. After the photocatalytic reaction, the suspension was filtered through a 1 kDa UF membrane to concentrate the microbial biomass for the quantification of gene copies, and the membranes were collected and stored at −20 °C. Then, DNA was isolated using a rapid soil genomic DNA extraction kit (MPBIO), and DNA purity and concentration were measured by means of an ultra-micro spectrophotometer (Thermo). Real-time qPCR was used to measure ARG absolute abundance. The specific details of the qPCR reaction system, including the used upstream and downstream primers, as well as the qPCR reaction procedures, are provided in Tables S2–S4.

3. Results and discussion

3.1. Characterization

With the use of scanning electron microscopy (SEM), the samples' surface morphology was investigated. The SEM images of g-C_3N_4, Bi_2WO_6, and the Bi_2WO_6/g-C_3N_4 composite materials are presented in Fig. 1a–d. The g-C_3N_4 structure (Fig. 1a) exhibited a typical blocky structure agglomerated by a lamellar structure, which provided favorable conditions for the loading of Bi_2WO_6. Bi_2WO_6 (Fig. 1b) displayed a flower-like structure formed by granular objects with a fluffy and porous surface. The uniform loading of Bi_2WO_6 crystals onto the g-C_3N_4 surface is demonstrated in Fig. 1c–d, which indicates the successful synthesis of Bi_2WO_6/g-C_3N_4 composites.

Microstructures underwent additional examination of the samples through TEM and HRTEM. Based on the SEM observation, the lamellar dark portion in Fig. 1e was corresponded to Bi_2WO_6, while the light part was linked to the g-C_3N_4 structure. This suggests that g-C_3N_4 is more than merely a physical blend of Bi_2WO_6 and g-C_3N_4, the strong binding between Bi_2WO_6 and g-C_3N_4 is seen in Fig. 1e, which enhances charge transfer and the separation efficiency of photogenerated carriers. The lattice fringe spacing in HRTEM (Fig. 1f) measured 0.315 nm, aligning with the (131) plane of Bi_2WO_6.[42]

Fig. 2 displays the N_2 adsorption–desorption isotherms and pore size distributions of g-C_3N_4 and its Bi_2WO_6 composite. Both materials display IV-type isotherms accompanied by H_3-type hysteresis loops. Key details regarding surface area and pore size distribution are outlined in Table S5. The specific surface area of g-C_3N_4 measures 8.052 m^2 g^{-1}, whereas the Bi_2WO_6/g-C_3N_4 composite boasts a significantly higher surface area of 46.430 m^2 g^{-1}. The relatively small surface area of g-C_3N_4 can be linked to its dense, block-like architecture. However, incorporating Bi_2WO_6 markedly boosts the specific surface area of Bi_2WO_6/g-C_3N_4 composites, a key factor in improving their photocatalytic efficiency.

The crystal phase of the samples was examined through XRD, where distinct peaks emerged at 2θ = 28.3°, 32.8°, 47.1°,

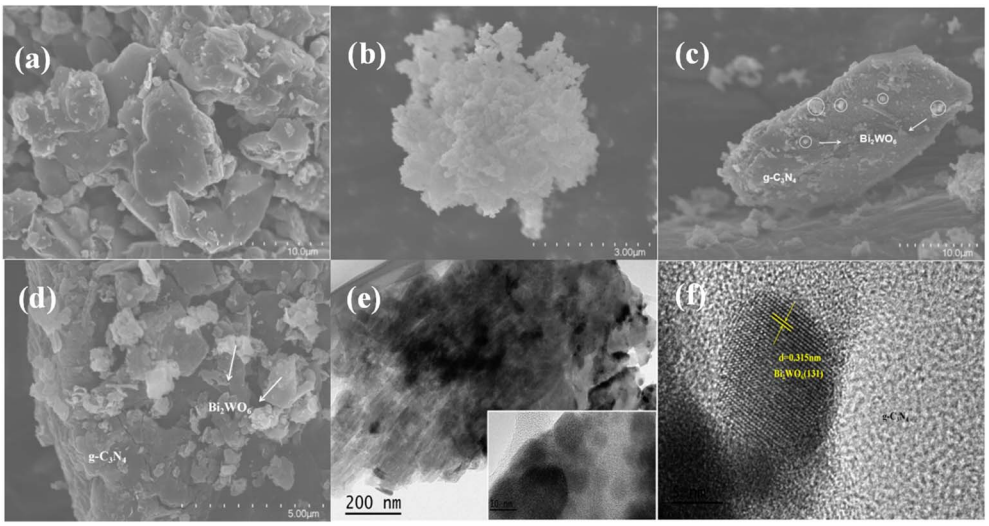

Fig. 1 SEM images of (a) g-C_3N_4, (b) Bi_2WO_6, and (c and d) Bi_2WO_6/g-C_3N_4 samples; (e) TEM image of Bi_2WO_6/g-C_3N_4 sample; (f) HRTEM image of Bi_2WO_6/g-C_3N_4 sample.

and 56.0°, corresponding to the (131), (200), (202), and (133) planes of the Bi_2WO_6 reference (JCPDS no. 39-0256), as depicted in Fig. 3a. Furthermore, peaks at $2\theta = 13.4°$ and 27.5° align with the (100) and (002) planes of the g-C_3N_4 reference (JPDS87-1526). These findings can be attributed to the well-ordered arrangement of tri-*s*-triazine rings and their interlayer stacking. While the Bi_2WO_6 diffraction peaks in the composite were relatively weak, the successful synthesis of the materials was unequivocally verified through complementary TEM and XPS analyses.

Fig. 3b illustrates the FTIR spectra for g-C_3N_4, Bi_2WO_6, and the composite material Bi_2WO_6/g-C_3N_4. A prominent peak at 810 cm^{-1} is linked to the bending vibrations of the tri-*s*-triazine unit found in g-C_3N_4.[43] The absorption bands in the range of 1240 to 1640 cm^{-1} are associated with the typical stretching vibrations of CN- and C=N heterocycles.[44] Additionally, the broad peaks observed between 3000 and 3300 cm^{-1} correspond to the stretching vibrations of –NH bonds.[45] Notably, Bi_2WO_6 displays significant absorption bands within the 500 to 800 cm^{-1} range, primarily tied to the Bi–O, W–O, and W–O–W bridging stretching modes.[46] The spectral characteristics of the composite closely resemble those of g-C_3N_4, indicating that the addition of Bi_2WO_6 preserves the fundamental structure of g-C_3N_4.

To analyze the optical properties of these materials, UV-vis diffuse reflectance spectroscopy (UV-vis DRS) was performed. As shown in Fig. 3c, g-C_3N_4 presents a clear absorption edge around 470 nm, corresponding to a bandgap of 2.73 eV. In comparison, Bi_2WO_6 demonstrates a pronounced absorption edge at 440 nm, indicating a bandgap of 2.82 eV. The Bi_2WO_6/g-C_3N_4 composite, on the other hand, exhibits enhanced visible light absorption with a red-shifted edge and a reduced bandgap of 2.69 eV, which is 0.04 eV smaller than that of pure g-C_3N_4. This alteration indicates the establishment of a heterojunction between Bi_2WO_6 and g-C_3N_4, which is essential for significantly enhancing the separation and transportation of photogenerated charge carriers. Consequently, the photocatalytic efficiency of the composite experiences a marked improvement.

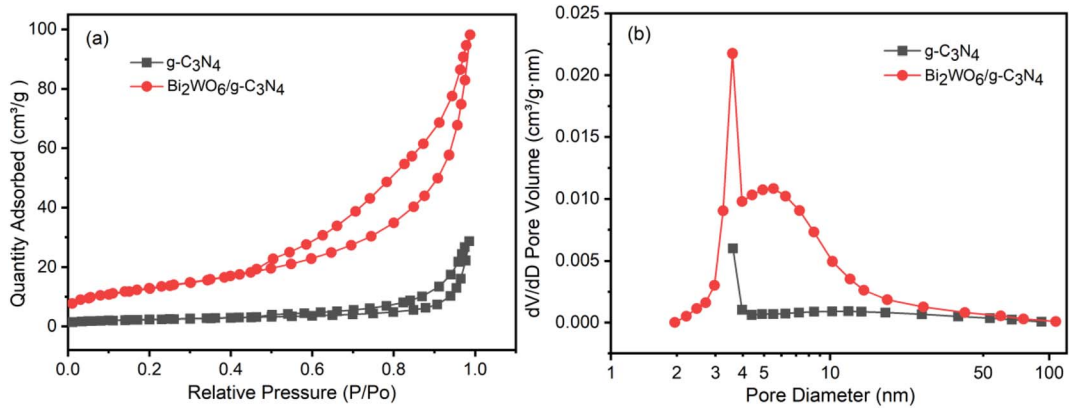

Fig. 2 (a) N_2 absorption–desorption isotherm and (b) pore size distribution of Bi_2WO_6/g-C_3N_4.

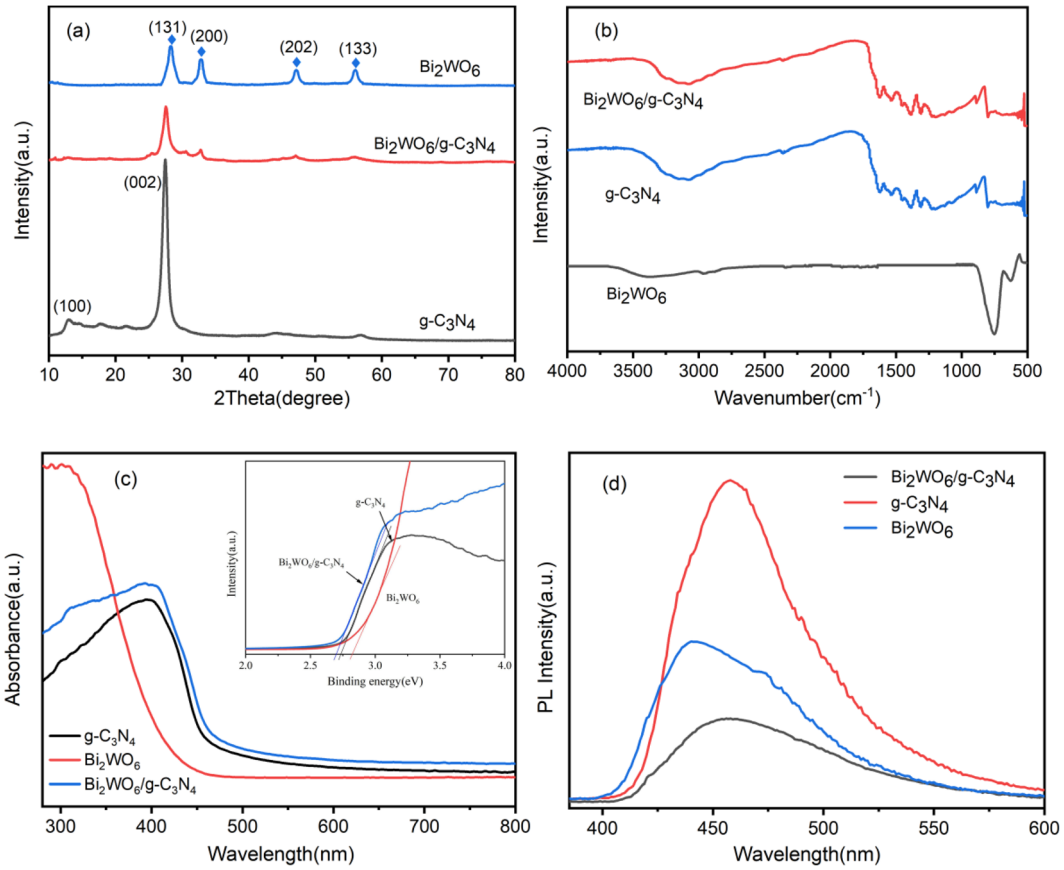

Fig. 3 (a) XRD pattern; (b) FT-IR spectra; (c) UV-vis diffuse reflection spectra (UV-vis DRS) and (d) photoluminescence (PL) emission spectra patterns of Bi_2WO_6, g-C_3N_4 and Bi_2WO_6/g-C_3N_4.

PL spectroscopy was used to analyze the dynamics of electron–hole pairs generated by light in semiconductors. A reduction in PL peak intensity signifies enhanced separation efficiency of these charge carriers. Fig. 3d demonstrates that g-C_3N_4 displays the highest photoluminescence peak intensity, indicating a significant recombination rate of photogenerated electrons and holes. Conversely, the Bi_2WO_6/g-C_3N_4 composite exhibits markedly reduced PL intensity relative to each individual component, indicating its efficacy in mitigating charge carrier recombination. This suppression improves the composite's photocatalytic degradation efficacy, rendering it more suitable for practical applications.

XPS was subsequently employed to examine the elemental makeup of the sample surface and its chemical state. Fig. 4a illustrates the complete XPS spectra of g-C_3N_4, Bi_2WO_6, and Bi_2WO_6/g-C_3N_4 composites. The distinctive peaks associated with the components C, N, O, W, and Bi were identified in the composites, confirming the effective synthesis of Bi_2WO_6/g-C_3N_4 composites. The C 1s spectrum of g-C_3N_4 was shown in Fig. 4b, which exhibited peaks at 281.3 eV for C–N/CO, 284.7 eV for surface ambiguous carbon C–C, 286.2 eV for C–(N_3), and 289.5 eV for C=N, respectively, all originating from different positions of the aromatic heterocycles in g-C_3N_4.[47,48] The C 1s peak of Bi_2WO_6/g-C_3N_4 composites corresponded to that of g-C_3N_4, but it exhibited a slightly increased binding energy and a new N–C=N peak at 288.3 eV. These observations indicated interactions among the composite material's components.

Fig. 4c showcases the detailed XPS spectra of the N 1s region for g-C_3N_4 and Bi_2WO_6/g-C_3N_4. In the case of g-C_3N_4, the N 1s spectrum reveals four distinct peaks positioned at 394.7 eV, 395.5 eV, 397.3 eV, and 399.8 eV. These peaks are attributed to pyridinic nitrogen, C–N bonds, sp^2-hybridized nitrogen atoms within the triazine structure (C=N–C), and tertiary N–C_3 configurations, respectively.[49,50] In comparison to g-C_3N_4, the binding energy of the corresponding N 1s peaks of Bi_2WO_6/g-C_3N_4 composites was increased, possibly owing to the interactions in the interaction of Bi_2WO_6 and g-C_3N_4, which led to changes in the electronic structure of the composites. Fig. 4d shows the O1s spectra of Bi_2WO_6 and Bi_2WO_6/g-C_3N_4 composites. The distinct peaks observed at 530.0 eV and 530.8 eV of Bi_2WO_6 corresponded to the Bi–O bond and Bi–O–W bond, respectively,[51] while the maximum at 532.2 eV is likely linked to O^2 adsorption during the preparation phase. In Bi_2WO_6/g-C_3N_4 composites, new spectral peaks at 531.8 eV and 532.8 eV were detected. These may be ascribed to the Bi–O–W bond and C–OH bond formed due to the presence of g-C_3N_4.

The high-resolution XPS spectra of Bi 4f (Fig. 4e) reveal distinct peaks at 159.9 eV (Bi $4f_{7/2}$) and 165.3 eV (Bi $4f_{5/2}$), which are attributed to the presence of Bi^{3+} in Bi_2WO_6.[52] Likewise, in the Bi_2WO_6/g-C_3N_4 composites, the peaks at 159.4 eV and

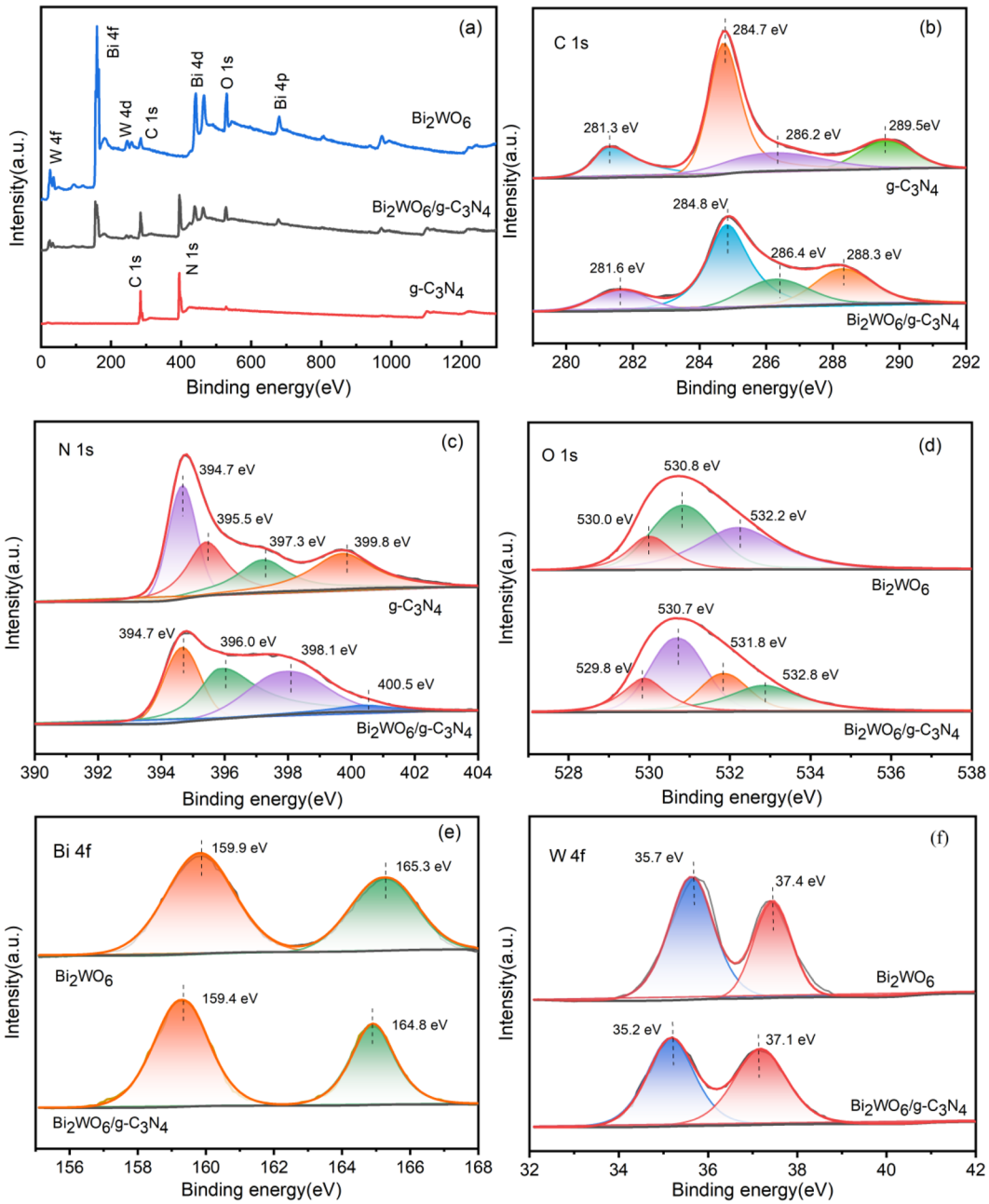

Fig. 4 X-ray photoelectron (a) survey, (b) C 1s, (c) N 1s, (d) O 1s, (e) Bi 4f and (f) W 4f spectrum of Bi_2WO_6, g-C_3N_4 and Bi_2WO_6/g-C_3N_4.

164.8 eV also align with Bi^{3+}, further confirming its presence. Turning to the W 4f spectra (Fig. 4f), the peaks observed in Bi_2WO_6 at 35.7 eV and 37.4 eV provide additional insights into the material's electronic structure. These findings collectively underscore the role of Bi^{3+} and the structural characteristics of the composite system. Along with the peaks observed at 35.2 eV and 37.1 eV in Bi_2WO_6/g-C_3N_4 composites, correspond to W^{6+} in the W $4f_{7/2}$ and W $4f_{5/2}$ states. Compared to Bi_2WO_6, the positions of the characteristic peaks in Bi_2WO_6/g-C_3N_4 composites decreased by 0.3–0.5 eV, indicating a significant interaction between g-C_3N_4 and Bi_2WO_6, rather than simple physical adsorption. This interaction facilitates the migration of photogenerated charge carriers between the surfaces of the composite material, thereby enhancing the photocatalytic efficiency of the composite material.

3.2. Photocatalysis degradation of TCs

To assess the photocatalytic efficacy of the Bi_2WO_6/g-C_3N_4 composite under visible light irradiation, the degradation efficiencies of various tetracyclines (TC, CTC, and OTC) were systematically investigated. As demonstrated in Fig. 5a, the degradation efficiency of TC without any catalyst can be neglected, indicating that TC did not undergo photolysis within 140 min. Under the photocatalysis of g-C_3N_4 and Bi_2WO_6 catalysts, only

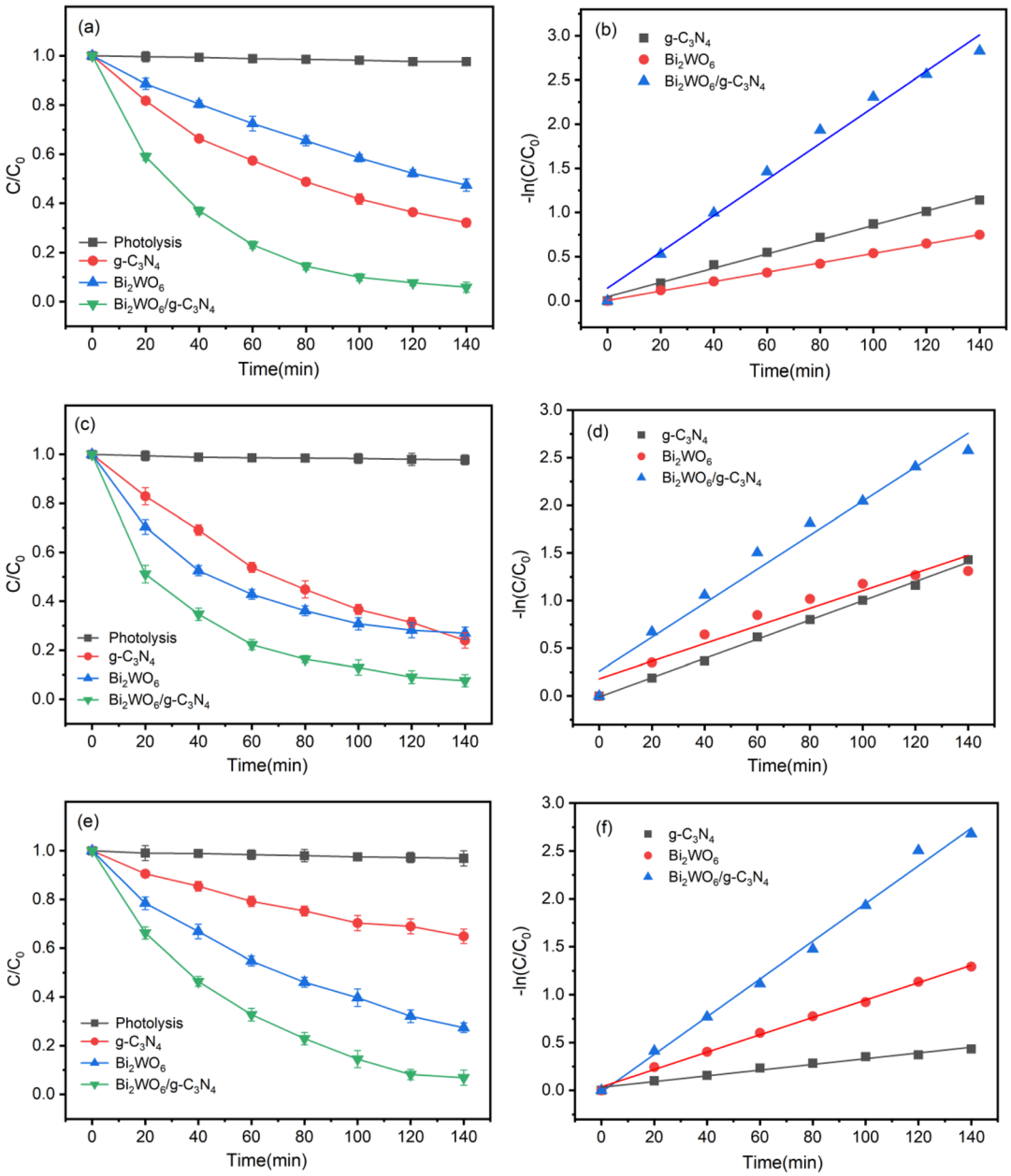

Fig. 5 Removal efficiency (a) and kinetics (b) for TC, removal efficiency (c) and kinetics (d) for CTC, and removal efficiency (e) and kinetics (f) for OTC under photocatalytic oxidation.

67.87% and 52.57% of TC were degraded, respectively. However, the photocatalytic efficiency of Bi_2WO_6/g-C_3N_4 is significantly notable, achieving a removal rate of 94.09% for TC under the same experimental circumstances. As illustrated in Fig. 5b, the degradation of TC followed a pseudo-first-order kinetic model. Notably, the rate constants for Bi_2WO_6/g-C_3N_4 outperformed those of Bi_2WO_6 and g-C_3N_4 by a significant margin, clocking in at 4.70 and 3.33 times higher, respectively. Similarly, consistent results were observed in the degradation of CTC and OTC. The degradation of CTC and OTC during individual visible light irradiation was minimal, as shown in Fig. 5c–e, indicating CTC and OTC did not undergo photolysis. After 140 minutes of photocatalytic reaction, the removal efficiencies of CTC and OTC by Bi_2WO_6/g-C_3N_4 were 92.39% and 93.15%, respectively, which were substantially higher than those of g-C_3N_4 and Bi_2WO_6. Notably, the removal rates of OTC by Bi_2WO_6/g-C_3N_4 were increased by 57.99% and 20.54%, severally, compared to g-C_3N_4 and Bi_2WO_6.

From Fig. 5d–f, it is evident that the Bi_2WO_6/g-C_3N_4 composites demonstrate high reaction rates for both CTC and OTC, as indicated by the specific kinetic constants in Table S6. Based on the above results, the Bi_2WO_6/g-C_3N_4 composite material demonstrated excellent photocatalytic removal efficiency for TCs. This is probably because the Bi_2WO_6/g-C_3N_4 composites effectively inhibit electron–hole recombination by forming heterojunctions, which improves photocatalytic oxidation performance and increases the utilisation of visible light.

3.3. Analysis of impact factors

3.3.1. The impact of catalyst dosage. The range of Bi_2WO_6/g-C_3N_4 catalyst was from 0.2 g L^{-1} to 1.5 g L^{-1} in the experiments. In Fig. 6a, the photocatalytic oxidation removal rate of TC increased from 81.80% to 94.09% as the catalyst dosage was increased from 0.2 g L^{-1} to 1.0 g L^{-1}. The improvement could be ascribed to the higher number of effective active sites on the surface of the photocatalytic material resulting from the increased catalyst dosage. Consequently, more photons were absorbed, leading to the generation of a greater number of active oxidants. Thereby the TC removal rate was enhanced. However, the impact on the TC removal rate decreased when the catalyst dosage was raised to 1.5 g L^{-1}. This might be explained by the light scattering brought on by high catalyst dosages, which affected the transmittance of the solution and subsequently reduced the efficiency of photocatalytic degradation. In addition, this also could be attributed to the fact that at a dosage of 1.0 g L^{-1}, all TC molecules had already reacted with the catalyst's active sites, resulting in no further increase in the removal rate with continued dosage increment. Thus, 1.0 g L^{-1} of the Bi_2WO_6/g-C_3N_4 catalyst dosage was picked for the following experiments.

3.3.2. The effect of TC concentration. The range of the initial TC concentration is 20 mg L^{-1} to 100 mg L^{-1}. In Fig. 6b, when the TC concentrations were 20 mg L^{-1}, 50 mg L^{-1}, 80 mg L^{-1} and 100 mg L^{-1}, the photocatalytic removal rates were 94.09%, 76.17%, 61.43% and 52.00%, respectively. When the concentration of TC increased, the effectiveness of TC degradation by Bi_2WO_6/g-C_3N_4 reduced. This may be attributed to that a higher concentration of TC requires more active free radicals for the photocatalytic degradation process with the continuous increase of pollutant concentration, which cannot be met under insufficient catalyst dosage of active substances. In addition, when the pollutant concentration was high enough, nearly all the active sites of Bi_2WO_6/g-C_3N_4 were occupied, hindering the continuation of photocatalytic reaction.

3.3.3. The effect of initial pH. In order to determine the solution's impact on TC degradation, its initial pH values were 3, 5, 7, 9, and 11. Bi_2WO_6/g-C_3N_4 composites' degrading efficiency on TC was comparatively steady for pH values between 5 and 9, as shown in Fig. 6c. At pH 7, the best degrading performance was noted, with a 92.58% clearance rate. The clearance rate dropped to just 74.58% at pH 11, while the TC degradation efficiency dropped to 88.72% at the initial pH of 3.

The diminished removal of TC within the strongly acidic environment (pH = 3) was ascribed to the elevated concentration of hydrogen ions (h^+) that reacted with $^{\bullet}O_2^-$ (eqn. (2) and (3)). And $^{\bullet}O_2^-$ has an important role in TC degradation, as a result, under very acidic conditions, TC degradation efficiency was reduced. Under strongly alkaline conditions (pH = 11), OH^- reacted with the photoinduced carrier h^+ to produce $^{\bullet}OH$ (eqn (4)), which has less oxidability than h^+ dose during the TC

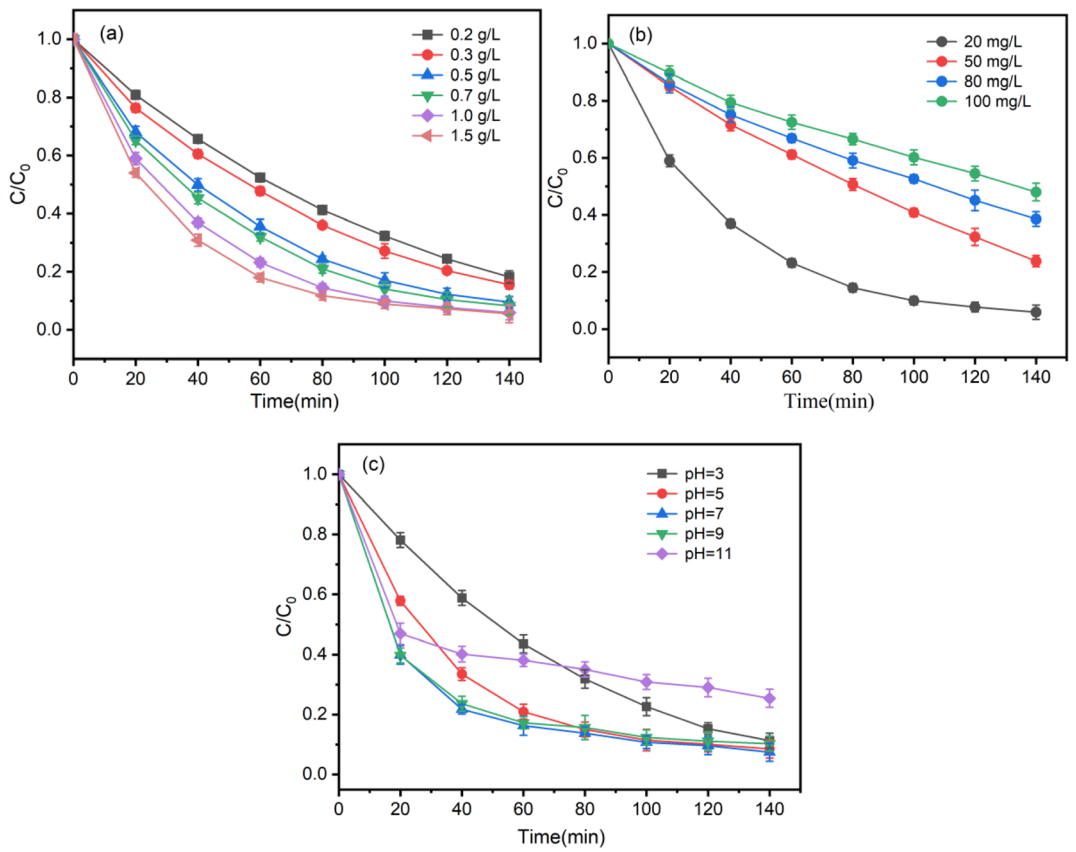

Fig. 6 Effects of (a) catalyst dosage, (b) pollutant concentration and (c) solution pH for the removal of TC by Bi_2WO_6/g-C_3N_4.

degradation. Furthermore, h^+ ions were the primary active species involved in the degradation of TC by Bi_2WO_6/g-C_3N_4 composites. According to the above mentioned analysis, the alkaline conditions had more significant effects for TC degradation reaction, and the neutral conditions were more favorable for the photocatalytic degradation of TC.

$$O_2 + e^- \rightarrow {}^{\cdot}O_2^- \quad (2)$$

$$2H^+ + {}^{\cdot}O_2^- + e^- \rightarrow H_2O_2 \quad (3)$$

$$OH^- + h^+ \rightarrow {}^{\cdot}OH \quad (4)$$

3.3.4. The effect of inorganic anions. The abundance of many inorganic anions in water complicates the pollution removal process. So the impact of common anions (Cl^-, SO_4^{2-} and HCO_3^-) on the degradation performance of TC was examined. Fig. S2a illustrates that with rising concentrations of anions, the efficiency of TC degradation steadily declined, indicating that anions hindered the degradation process of TC. As the Cl^- concentration rose from 0 mM to 10 mM, the photocatalytic efficiency of TC decreased from 94.09% to 90.70%. This might be the consequence of Cl^- and TC's competing adsorption on the catalyst surface, which could lower TC's degradation efficiency.[53]

Compared to Cl^-, SO_4^{2-} and HCO_3^- had more significant inhibitory effects to TC degradation efficiency (Fig. S2b and c). When the concentrations of SO_4^{2-} and HCO_3^- were both 10 mM, the removal rates of TC were reduced to 87.59% and 80.05%, respectively. According to previous reports,[54] SO_4^{2-} and HCO_3^- are scavengers of ${}^{\cdot}OH$ radical. In addition, HCO_3^- could also react with h^+ radical, leading to the decrease of active species involved in TC photocatalytic degradation. The corresponding reaction equations are as follows:

$$SO_4^{2-}/HCO_3^- + {}^{\cdot}OH \rightarrow {}^{\cdot}SO_4^-/{}^{\cdot}CO_3^- + H_2O \quad (5)$$

$$HCO_3^- + h^+ \rightarrow {}^{\cdot}CO_3^- + H^+ \quad (6)$$

$$SO_4^{2-} + h^+ \rightarrow {}^{\cdot}SO_4^- \quad (7)$$

In the aforementioned reactions, SO_4^{2-} and HCO_3^- are capable of reacting with reactive species to generate sulfate radicals (${}^{\cdot}SO_4^-$) and carbonate radicals (${}^{\cdot}CO_3^-$), respectively. In particular, ${}^{\cdot}CO_3^-$ serves as an oxidizing agent.[55] Theoretically, it required a longer duration for ${}^{\cdot}SO_4^-$ and ${}^{\cdot}CO_3^-$ to react with TC compared with h^+, and the oxidation ability for TC was weaker, which slows the rate of TC degradation.

3.3.5. The effect of HA. Fig. S2d demonstrates a gradual decline in TC's photocatalytic efficiency as HA concentration rises. Specifically, when the HA concentration rose from 0 mg L^{-1} to 10 mg L^{-1}, the removal efficiency of TC dropped from 94.09% to 85.35%. Firstly, this may result from the competition between HA and TC for active species during the photocatalytic process. Furthermore, HA also competed with Bi_2WO_6/g-C_3N_4 for photons, leading to fewer reactive oxygen species produced by photocatalysis. Although HA present, which somewhat hindered the breakdown of TC, the photocatalytic efficiency remained impressive, clocking in at over 85% even at an HA concentration of 10 mg L^{-1}. This clearly demonstrates the outstanding photocatalytic oxidation capabilities of the Bi_2WO_6/g-C_3N_4 composite material.

3.4. Reusability and practical applicability

3.4.1. Recycling performance. The reusability of catalysts is crucial for practical applications. Five recycling tests were performed to evaluate the durability and reusability of Bi_2WO_6/g-C_3N_4 composites in TC photocatalytic degradation. After completing the photocatalytic experiment, the catalyst was isolated from the reaction mixture, thoroughly rinsed three times using a combination of deionized water and ethanol, allowed to dry, and subsequently recycled for use in the next round of testing. Fig. 7 shows that after five consecutive reuses, 85.49% of the TC could be removed by the composite material, indicating that it maintained a high level of photocatalytic activity. As shown in Table S7, comparative analysis indicates that the Bi_2WO_6/g-C_3N_4 composite exhibits stability comparable to or even superior to numerous reported photocatalysts under identical cycling conditions, demonstrating exceptional reusability. The minor decline in degradation efficiency could stem from TC byproducts accumulating on the catalyst surface, reducing the number of active sites available for ROS generation.

To evaluate the structural stability and interfacial electronic properties of the Bi_2WO_6/g-C_3N_4 composite after repeated photocatalytic reactions, XPS analysis was performed on the used catalyst. As shown in Fig. S3a, the survey spectrum still contains the characteristic signals of Bi, W, O, C and N, indicating that the elemental composition remained unchanged obviously after cycling. The C 1s spectrum (Fig. S3b) shows peaks at ~284.8, ~286.2 and ~288.3 eV, corresponding to C–C/C=C, C–NH_x and the typical sp^2-hybridized N–C=N structure of g-C_3N_4, confirming the integrity of the conjugated framework. The N 1s spectrum (Fig. S3c) exhibits characteristic

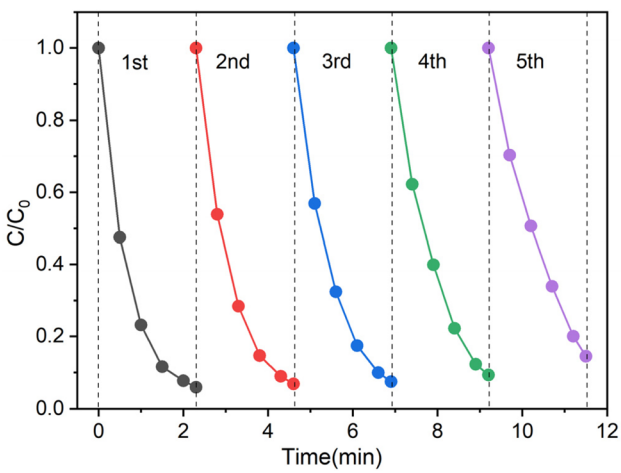

Fig. 7 Recyclability of Bi_2WO_6/g-C_3N_4 composites for photocatalytic degradation of TC.

components of C–N=C, N–(C)$_3$, C–N–H and π–π* transitions, further demonstrating the structural stability of g-C_3N_4. In the O 1s spectrum (Fig. S3d), the peak at ~529.8 eV is assigned to lattice oxygen (Bi–O/W–O), while the peaks at ~531.8 and ~532.8 eV are attributed to surface hydroxyl groups/oxygen defects and adsorbed oxygen species, respectively, indicating that the Bi_2WO_6 lattice structure was well preserved. The Bi 4f peaks at ~159.4 and ~164.8 eV (Fig. S3e) and the W 4f peaks at ~35.2 and ~37.1 eV (Fig. S3f) correspond to Bi^{3+} and W^{6+}, respectively, with no additional reduced species observed, confirming the chemical stability of the composite. Compared with the fresh catalyst, Bi 4f and W 4f exhibit slight negative shifts, while C 1s and N 1s show positive shifts, indicating electron migration from g-C_3N_4 to Bi_2WO_6 and the formation of stable interfacial charge redistribution. This directional electron transfer is consistent with a Z-scheme charge transfer pathway, in which electrons accumulate on Bi_2WO_6 and holes remain on g-C_3N_4. The persistence of this interfacial electronic interaction after cycling explains the excellent long-term stability of the Bi_2WO_6/g-C_3N_4 photocatalyst.

3.4.2. Influence of water matrix. When contemplating the application within real-life water scenarios, the water matrix constitutes a pivotal parameter. The removal rates of TC, CTC and OTC by Bi_2WO_6/g-C_3N_4 were investigated under various water sources, respectively. As illustrated in Fig. S4a, after 140 minutes of photocatalytic reaction, TC removal rates reached 94.19% in deionized water, 87.14% in tap water, and 86.73% in lake water. TC maintained high removal efficiency in tap and lake water, though slightly reduced compared to deionized water. Similarly, the removal efficiency of CTC, OTC in tap water and lake water was also slightly inhibited (Fig. S4b and c). In the lake water, the removal rates of CTC and OTC were 80.17% and 80.82%, respectively. Obviously, there were the lowest removal rates of TCs in lake water. This was mainly because there were large amounts of organic matter (NOM) in natural water, which would consume reactive species (ROS).[56,57] In addition, NOM can adsorb onto and strongly adhere to the photocatalyst surface, preventing light penetration and thus inhibiting ROS generation. Despite this, the elimination rates of TCs in natural water consistently exceeded 80%, demonstrating that the Bi_2WO_6/g-C_3N_4 composites exhibit remarkable photocatalytic oxidation efficiency and are not limited by the specific composition of the water matrix.

3.5. Photocatalytic mechanism

3.5.1. Role of active species. To pinpoint the main reactive species responsible for the photocatalytic degradation of TC, experiments incorporating radical scavengers were conducted. IPA, EDTA-2Na, and TEMPOL were employed as trapping agents to specifically capture $^{\bullet}OH$, h^+ and $^{\bullet}O_2^-$, respectively. This approach allowed for a clear identification of the primary contributors to the degradation process. As illustrated in Fig. 8, the findings revealed that introducing IPA had a negligible impact on TC degradation, showing less than a 5% reduction. This indicates that $^{\bullet}OH$ radicals had a limited, if any, role in TC degradation, suggesting they were not the primary reactive species responsible for the process. However, the degradation of TC was markedly suppressed when EDTA–2Na and TEMPOL were added, with TC removal reduced by 71.55% and 52.63%, respectively. These results suggested that h^+ was the primary active species in TC's photocatalytic degradation, with $^{\bullet}O_2^-$ functioning as a secondary active species of significance.

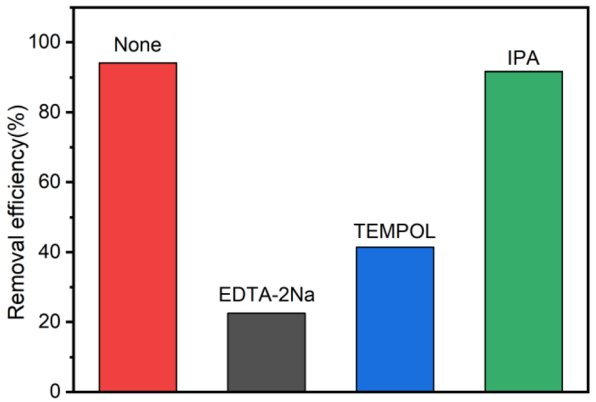

Fig. 8 Active species removal experiments for the degradation of TC.

The EPR spectra (Fig. 9a and b) provided further evidence of ROS involvement in the photocatalytic reaction. In the absence of light, no notable peaks were observed. However, upon light exposure, distinct signal peaks corresponding to DMPO–$^{\bullet}O_2^-$ and DMPO–$^{\bullet}OH$ adducts emerged, displaying an intensity ratio of 1 : 2 : 2 : 1. These findings confirm the production of $^{\bullet}OH$ and $^{\bullet}O_2^-$ radicals as part of the photocatalytic mechanism.

3.5.2. Electrochemical measurement. To delve deeper into the electron transfer characteristics of g-C_3N_4 and the Bi_2WO_6/g-C_3N_4 composite, we conducted a suite of electrochemical assessments. These experiments, encompassing transient photocurrent response (I–t) measurements and electrochemical impedance spectroscopy (EIS) analyses, shed light on how the materials perform under different scenarios, offering crucial insights into their functionality. As illustrated in Fig. 9c, the photocurrent density test was performed in 20 s cycles under alternating dark and light conditions. The research demonstrated that the Bi_2WO_6/g-C_3N_4 composite significantly outperformed g-C_3N_4 on its own, delivering a photocurrent response under visible light that was approximately 2.26 times higher. This impressive improvement underscored the composite's superior ability to suppress the recombination of electron–hole pairs generated by light, thereby extending the lifespan of charge carriers. Clearly, the Bi_2WO_6/g-C_3N_4 combination proved to be a game-changer in enhancing photocatalytic efficiency. The incorporation of heterojunctions in the Bi_2WO_6/g-C_3N_4 composites played a pivotal role in enhancing the separation efficiency of photogenerated carriers and accelerating electron transfer rates. These improvements directly contributed to the overall boost in photocatalytic performance.

In EIS, a smaller arc radius typically signals reduced charge transfer resistance and a more rapid interfacial charge transfer rate. As shown in Fig. 9d, the Bi_2WO_6/g-C_3N_4 composites demonstrated a significantly smaller arc radius compared to

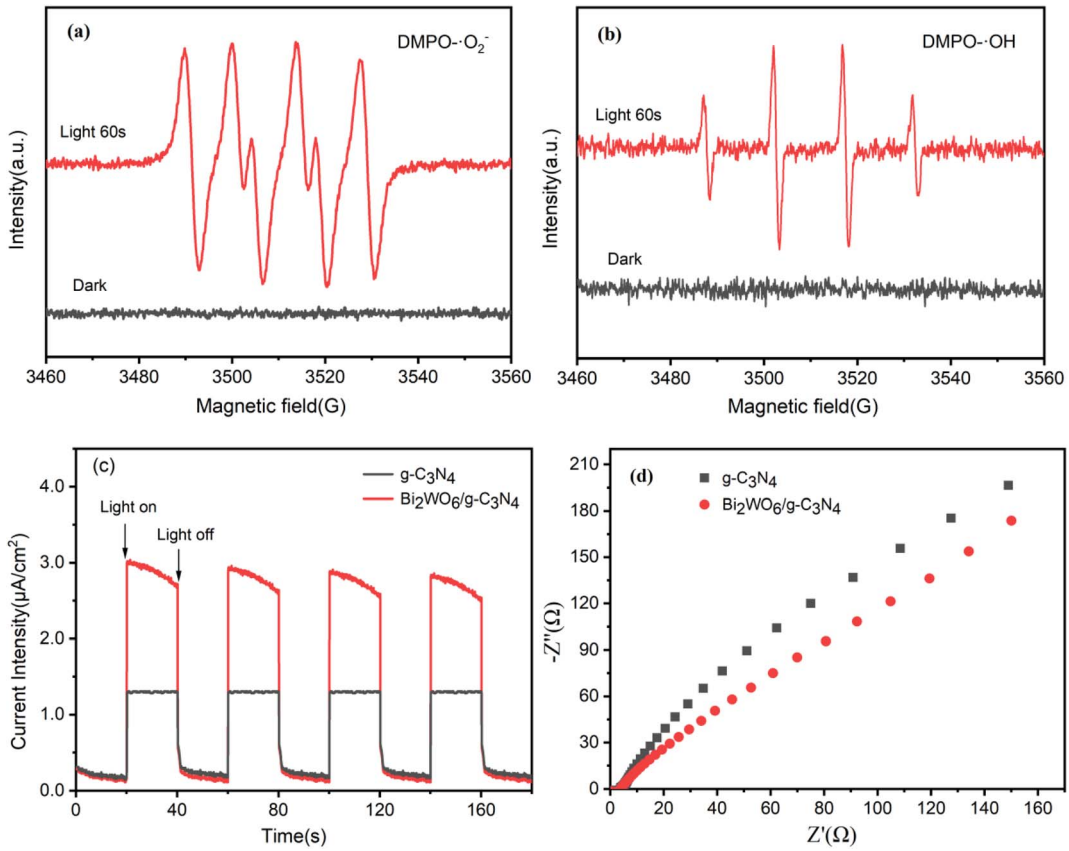

Fig. 9 EPR spectra of (a) DMPO–$^{\bullet}O_2^-$ and (b) DMPO–$^{\bullet}$OH; (c) transient photocurrent response and (d) electrochemical impedance spectroscopy of g-C_3N_4 and Bi_2WO_6/g-C_3N_4.

other samples, highlighting their superior ability to separate photogenerated charge carriers and facilitate faster charge transfer across the interface. This suggests enhanced efficiency in the material's electrochemical performance. To sum up, the electrochemical findings highlight that combining g-C_3N_4 with Bi_2WO_6 not only broadens the light absorption range but also minimizes the recombination of photogenerated carriers, offering a promising strategy to boost photocatalytic efficiency.

3.5.3. Photocatalytic degradation mechanism. Drawing from the experimental results described above, we propose a reaction mechanism for the photocatalytic breakdown of TC using Bi_2WO_6/g-C_3N_4 composites. As depicted in Fig. 10a, the overlapping band structures of g-C_3N_4 and Bi_2WO_6 semiconductors are well-matched. When visible light hits these composites, electrons in the VB of both semiconductors gain energy and jump into their corresponding CB, creating holes in the VB. Given that the CB potential of g-C_3N_4 is significantly lower at −1.23 eV compared to Bi_2WO_6 at 0.45 eV, electrons from the CB of g-C_3N_4 tend to move toward the CB of Bi_2WO_6. Conversely, the VB potential of Bi_2WO_6, which stands at 3.27 eV, is much higher than that of g-C_3N_4 at 1.50 eV, allowing holes in Bi_2WO_6's VB to readily shift to g-C_3N_4's VB. This interplay facilitates the effective separation of photogenerated charge carriers—with electrons accumulating in the CB of Bi_2WO_6 and holes forming in the VB of g-C_3N_4. Nonetheless, the higher CB potential of Bi_2WO_6, compared to the reduction potential of the O_2/$^{\bullet}O_2^-$ pair (−0.33 eV), prevents oxygen molecules on the catalyst surface from being reduced to $^{\bullet}O_2^-$ by electrons. This observation directly contradicts findings from active species capture experiments and previous EPR results. Consequently, the charge separation mechanism within the Bi_2WO_6/g-C_3N_4

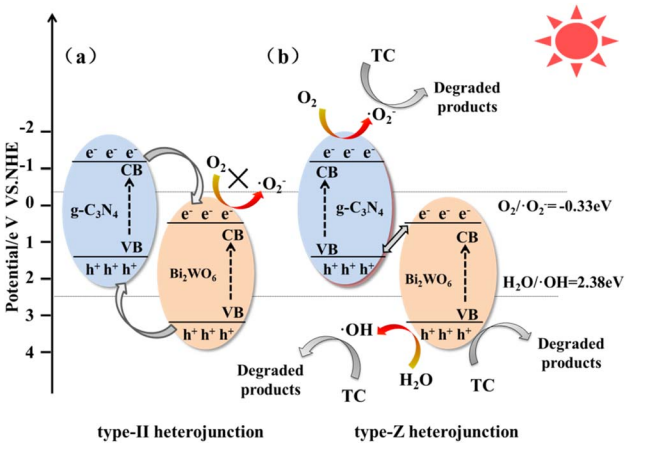

Fig. 10 Photocatalytic degradation mechanism of TC by Bi_2WO_6/g-C_3N_4 composites; (a) type-II heterojunction, (b) type-Z heterojunction.

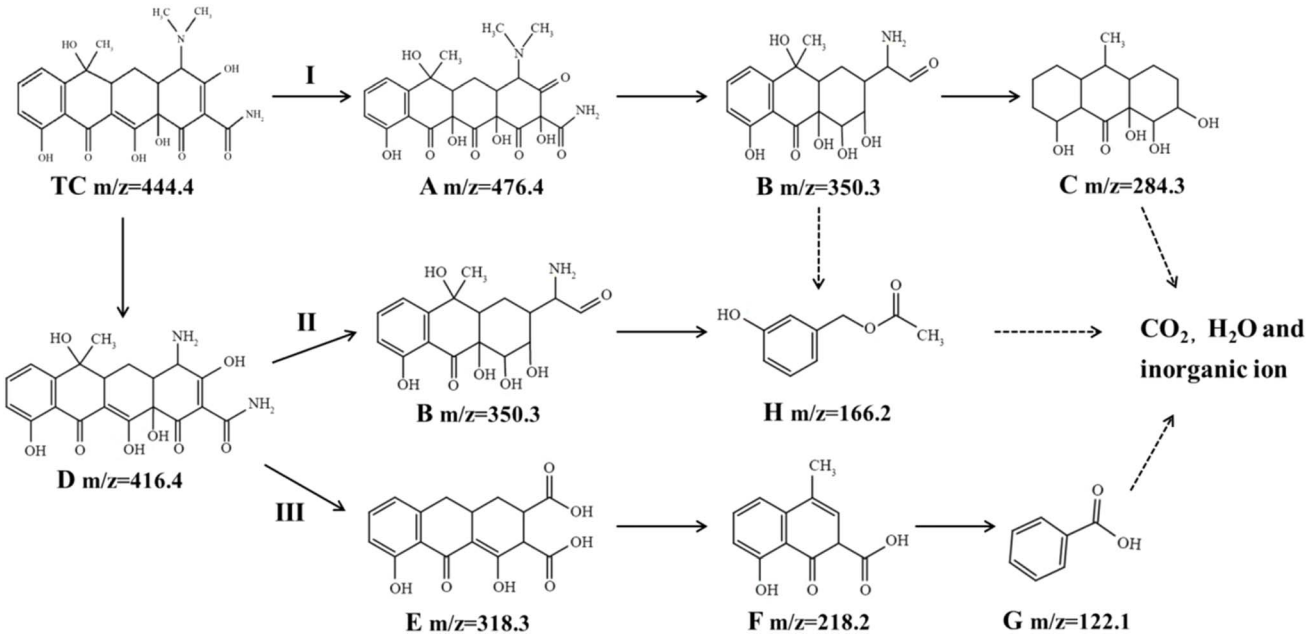

Fig. 11 Degradation pathways of TC degradation products.

system does not align with the conventional type-II heterojunction model.

Based on the result above, a photogenerated carrier separation mechanism based on type-Z heterojunction was proposed as illustrated in Fig. 10b. When Bi_2WO_6 and g-C_3N_4 are brought into close proximity, they form an internal electric field at their interface. This electric field facilitates the recombination of electrons from Bi_2WO_6's conduction band with holes from g-C_3N_4's valence band. Additionally, g-C_3N_4 plays a crucial role in reducing adsorbed O^2 molecules on the catalyst's surface to $^{\bullet}O_2^-$, thanks to its conduction band potential (−1.23 eV) being notably lower than the redox potential required for converting O_2 to O_2^- (−0.33 eV). This capability is key to promoting the transformation of surface-adsorbed oxygen into $^{\bullet}O_2^-$. On the other hand, Bi_2WO_6's VB potential (3.27 eV) surpasses that of $H_2O/^{\bullet}OH$ (2.37 eV), enabling it to utilize holes from its valence band to oxidize a fraction of water molecules into $^{\bullet}OH$. These findings are corroborated by EPR spectroscopy and active species trapping experiments, which highlight h^+ and $^{\bullet}O_2^-$ as the primary active species driving TC degradation. Consequently, the type-Z heterojunction formed between Bi_2WO_6 and g-C_3N_4 in this study is pivotal for the efficient separation of photogenerated charge carriers, thereby significantly boosting the composite's photocatalytic performance.

3.5.4. Possible degradation intermediates and pathways. Given the structural resemblance among TCs,[58] TC was chosen as the model compound to explore degradation intermediates and pathways. Its reaction products were identified using HPLC-MS. During the photocatalytic process, eight intermediates were initially pinpointed (Table S8 and Fig S5–S7). Based on detection, the photocatalytic degradation process for TC mainly underwent the demethylation reaction, deamidation reaction, ring opening reaction and oxidation reaction.[59]

There were three degradation pathways for the degradation reaction of TC, which were presented in Fig. 11. In pathway I, the combined action of h^+ and $^{\bullet}O_2^-$ facilitated the conjugation of –C═C– to the neighboring –OH in TC. The –OH acted as the electron donor made the –C═C– linkage weaker and became a site vulnerable to attack by free radicals. Therefore, TC (m/z = 444.4) reacted with hydroxyl addition and oxidation to generate product A (m/z = 476.4). And then, product A was further oxidized to product B (m/z = 350.3) by dehydration, demethylation, deamidation and ring opening reactions. Subsequently, under a series of attacks by ROS, the product was eventually oxidized to the small molecule products C (m/z = 284.3) and H (m/z = 166.2). As a result of ROS attack, the N–C bond with lower energy in TC broke and underwent demethylation reaction to generate product D (m/z = 416.4). Subsequently, in pathway II, the product B (m/z = 350.3) was converted from product D by deamidation, addition reactions and ring opening, and finally oxidized to the small molecule product H (m/z = 166.2). In pathway III, the product E (m/z = 318.3) was generated from product D by the reactions of deamidation, demethylation and ring opening. In the presence of ROS, by reactions such as decarboxylation and ring opening, the product E was further oxidized to small molecules F (m/z = 218.2) and G (m/z = 122.1). Eventually, some of the small molecules generated were converted to CO_2 and H_2O by the carbonation reaction.

3.6. Photocatalytic inactivation of ARGs

3.6.1. Degradation performance of ARGs. The potentiality of Bi_2WO_6/g-C_3N_4 photocatalyst applied in the inactivation of ARGs was investigated by tetracycline and sulfonamide ARGs as targets. Fig. 12a shows that the absolute abundances of *16S rRNA*, *intI*, *sulI*, *sulII*, *tetA* and *tetC* in the treated wastewater from the plant were $10^{8.59}$, $10^{7.23}$, $10^{7.34}$, $10^{7.19}$, $10^{6.16}$ and $10^{4.53}$

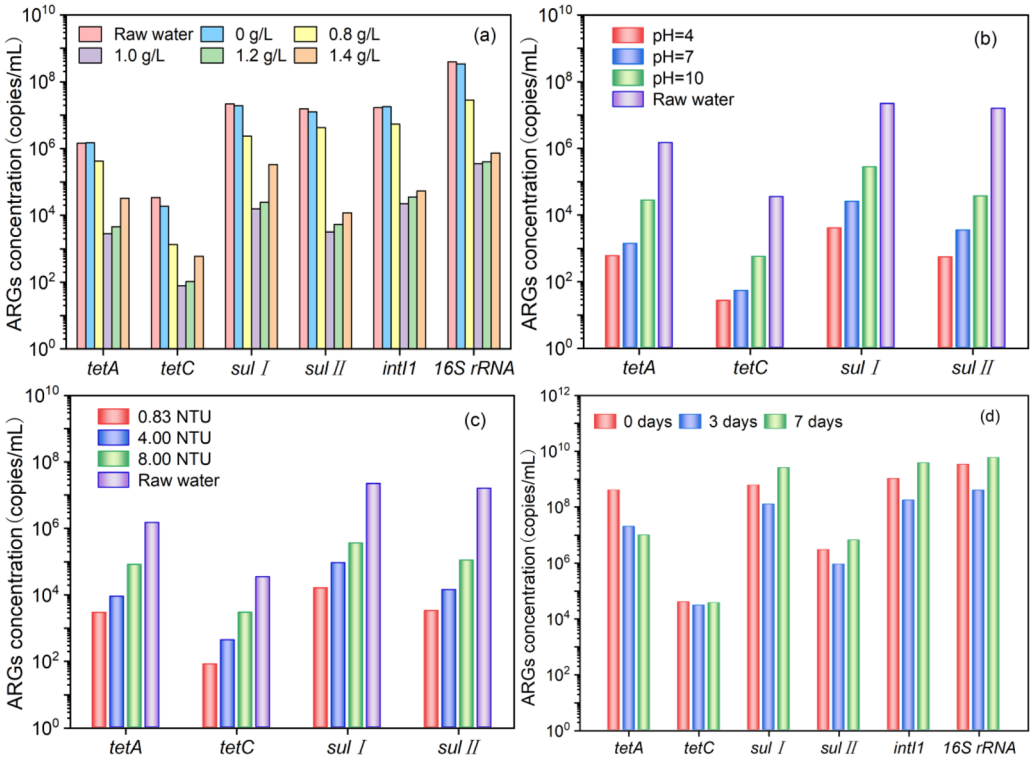

Fig. 12 (a) Removal of ARGs with different catalyst dosages; effect of (b) initial pH and (c) turbidity on ARGs removal; (d) regeneration of ARGs at different times.

copies per mL, respectively. This indicated that the effluent still contained a large amount of ARGs even after treatment by the wastewater plant. If discharged directly, it could present a threat to human health and ecosystems.

As shown in Fig. 12a, the concentration of different types of ARGs in water showed a pattern of initially declining and then rising as the Bi_2WO_6/g-C_3N_4 dosage increased. The concentration of ARGs remained relatively constant in the light control group, indicating that direct light had little to no effect on the removal of ARGs. When the dose of Bi_2WO_6/g-C_3N_4 was 1.0 g L^{-1}, the ARGs removal performance was effective. The removal ratios of *16S rRNA*, *intI1*, *tetA*, *tetC*, *sulI* and *sulII* were 3.04 log, 2.88 log, 3.15 log, 3.68 log, 2.71 log and 2.64 log, respectively. However, with the further increase of the Bi_2WO_6/g-C_3N_4 dose, the removal effect of ARGs did not appear to be significantly improved. This may be due to the overdosing of the catalyst, which affected the translucency of the solution and reduced the generation of reactive radicals, subsequently decreasing the removal of ARGs. The best removal of ARGs was achieved at the Bi_2WO_6/g-C_3N_4 dosage of 1.0 g L^{-1}. Therefore, the optimal dosage was found to be 1.0 g L^{-1} in this study and selected for subsequent experiments. In summary, Bi_2WO_6/g-C_3N_4 has excellent photocatalytic oxidation performance and effectively removes ARGs from wastewater plant secondary effluent.

3.6.2. Impact factors. It has been shown that pH and turbidity are two important factors in the photocatalytic treatment of ARGs. Therefore, the initial pH and turbidity of the secondary effluent were varied during the experiments, to evaluate the effectiveness of ARGs removal using Bi_2WO_6/g-C_3N_4 photocatalysis across various conditions. In Fig. 12b, the efficiency of photocatalytic oxidation in removing ARGs declines as pH levels rise. When pH was 4, after 140 min of photocatalytic reaction, the concentrations of *tetA*, *tetC*, *sulI* and *sulII* in the water were $10^{2.76}$, $10^{1.41}$, $10^{3.58}$ and $10^{2.72}$ copies per mL, respectively. However, when pH was 10, the concentrations of ARGs increased significantly to $10^{4.43}$, $10^{2.74}$, $10^{5.43}$ and $10^{4.55}$ copies per mL, respectively. This phenomenon could be attributed to the rate constant of the visible photolysis reaction, which took a nosedive as the pH of the water sample climbed, resulting in a dip in the photodegradation efficiency of ARGs.

The raw water turbidity of the secondary effluent was 0.83 NTU, which was adjusted to 4.00 NTU and 8.00 NTU by adding kaolin clay, respectively. With reference to the Fig. 12c, the oxidation effect of Bi_2WO_6/g-C_3N_4 on ARGs decreased with an increase in turbidity. The best removal of ARGs was achieved when the turbidity was 0.83 NTU. However, when the turbidity increased to 8.00 NTU, the concentration of ARGs increased significantly, with *tetA*, *tetC*, *sulI* and *sulII* concentrations of $10^{4.90}$, $10^{3.46}$, $10^{5.55}$ and $10^{5.03}$ copies per mL, respectively. This might be attributed to excessive turbidity of the water sample affects the solution light transmission, resulting in less active radicals produced by the photocatalytic reaction, which reduced the removal rate of ARGs.

3.6.3. The regeneration of ARGs. The regeneration performance of ARGs treated with Bi_2WO_6/g-C_3N_4 photocatalyst was investigated. Fig. 12d shows the concentration changes of ARGs

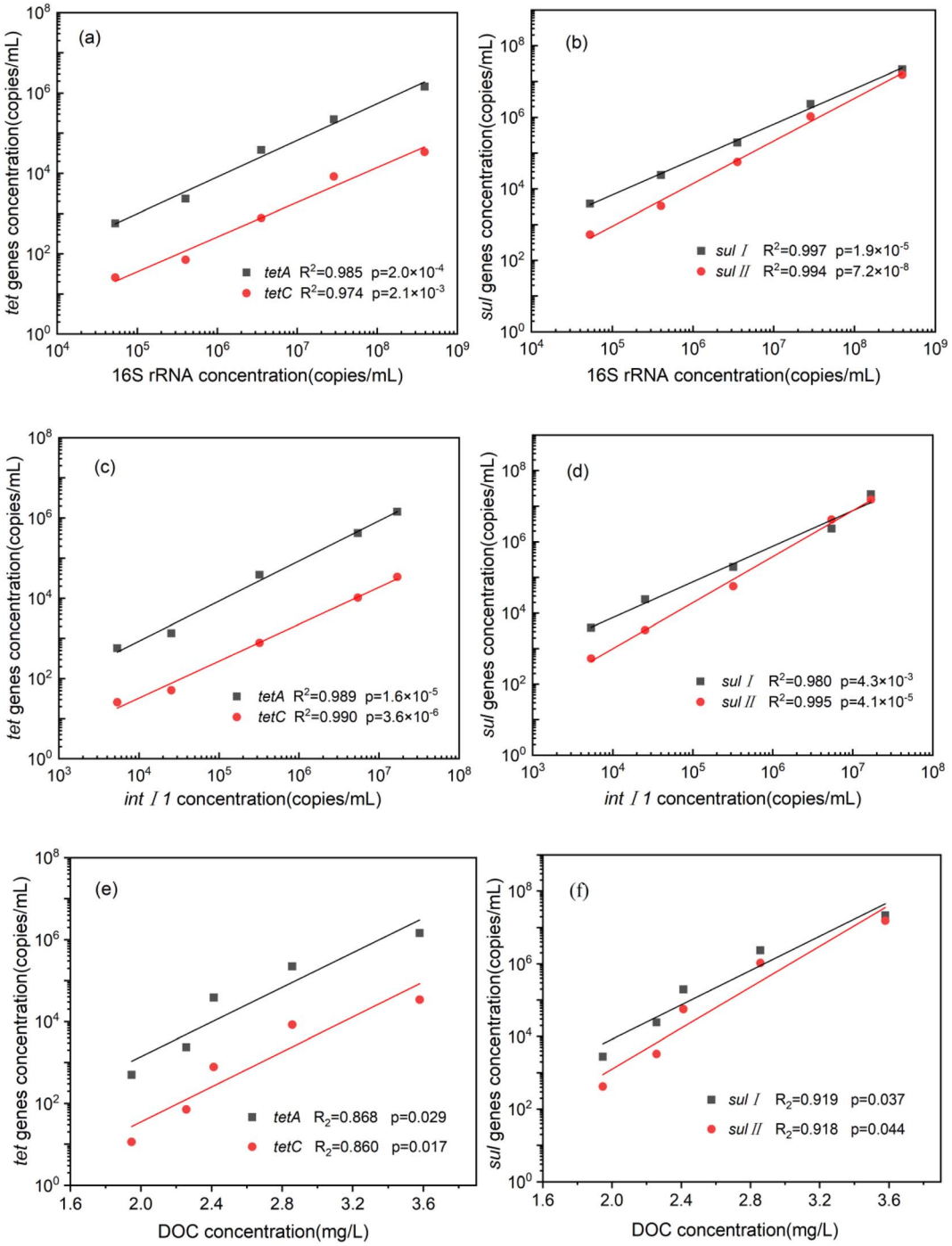

Fig. 13 *tetA* and *tetC*, (b) *sul*I and *sul*II, *intI1* and (c) *tetA* and *tetC*, (d) *sul*I and *sul*II , DOC and (e) *tetA* and *tetC*, (f) *sul*I and *sul*II.Correlations between 16S rRNA and (a) *tetA* and *tetC*, (b) *sulI* and *sulII*, *intI1* and (c) *tetA* and *tetC*, (d) *sulI* and *sulII*, *DOC* and (e) *tetA* and *tetC*, (f) *sulI* and *sulII*.

after photocatalytic treatment, as well as after being placed in the dark for 3 and 7 days. The findings indicated no recovery in ARG concentration following a 3-day dark place, but instead showed varying degrees of decrease.

However, the concentration of some ARGs increased after 7 days. The concentrations of *sulI*, *sulII*, *intI1* and *16S rRNA* increased to $10^{9.40}$, $10^{6.81}$, $10^{9.58}$ and $10^{9.77}$ copies per mL, respectively. The concentrations were 4.22, 2.24, 3.65 and 1.74 times higher than those at the end of photocatalysis. This may be due to the fact that the target ARGs host can repair and regrow within a certain period of time after photocatalytic treatment, while photocatalysis may cause damage to the host cell membrane, promoting horizontal transfer of ARGs and further leading to their proliferation.

3.6.4. Correlation analysis. Employing the linear regression methodology, the associative relationships between the

elimination of dissolved organic carbon (DOC), integron-associated gene intI1, 16S *rRNA*, tetracycline – resistance genes (*tetA* and *tetC*), and sulfonamide – resistance genes (*sulI* and *sulII*) within water samples were subjected to in-depth investigation. As illustrated in Fig. 13, there was a notable positive correlation ($p < 0.05$) detected among *16S rRNA*, *intI1*, DOC, *tet* genes, and *sul* genes, with good fitting results. These indicated that with the removal of *16S rRNA*, *intI1* and DOC, the concentration of the four ARGs also decreased significantly.

As illustrated in Fig. 13a and b, there was a significant positive correlation between ARGs and *16S rRNA*. *16S rRNA* is ribosomal RNA that can identify microbial species and can be used to characterize the total microbial content in water samples. In particular, microbes were the expression sites of ARGs, and their presence led to the transfer and diffusion of ARGs. Moreover, the ROS generated by photocatalytic oxidation can destroy the cell structure of microorganisms and invade the inside of cells to destroy genetic material, thereby inactivating microbial. Therefore, the reduction of total microbial contributed to the reduction of ARGs concentration.

Integrons play a vital role in the dissemination of ARGs across various species in the environment. A significant portion of these ARGs in the ecosystem is housed in genetic transfer elements that enable the movement of resistance traits both among bacteria and within their own communities.[60] As shown in Fig. 13c and d, there were significant positive correlations between *tet* genes, *sul* genes and *intI1* genes, which implied that *tetA*, *tetC*, *sulI*, *sulII* might be bound to *intI1* in water samples. Consequently, the elimination of *intI1* was conducive to the decrease of ARGs.

ARGs can usually interact with organic matter and be removed from the wastewater together with organic colloidal particles.[61] The organic matters can be removed by photocatalytic technology, and the removal of organic material contributes to the reduction of ARGs (Fig. 13e and f). In addition, DOC is a nutrient necessary for the survival of heterotrophic bacteria, and its concentration reduction can inhibit the growth and reproduction of bacteria, thus inhibiting the propagation of ARGs to some extent. To sum up, the removal of *16S rRNA*, *intI1,* and DOC in secondary effluents is of great significance for reducing ARGs.

4. Conclusions

A novel Bi_2WO_6/g-C_3N_4 catalyst has been constructed by this study. The key to boosting photocatalytic prowess was the efficient separation of electron–hole pairs generated by light within the Bi_2WO_6/g-C_3N_4 heterojunction. Compared with pure g-C_3N_4 and Bi_2WO_6, the removal efficiency of the Bi_2WO_6/g-C_3N_4 composite material increased by approximately 38.6% and 79.0%, respectively. The removal rates of TC, CTC and OTC were 94.09%, 92.39% and 93.15% in 140 min, respectively. It maintained an 84.59% removal rate even after five cycles. At a Bi_2WO_6/g-C_3N_4 dosage of 1.0 g L^{-1}, the removal efficiencies of 16S rRNA, intI1, tetA, tetC, sulI, and sulII reached 3.04, 2.88, 3.15, 3.68, 2.71, and 2.64 log, respectively. Quenching experiments identified h^+ and $^{\bullet}O_2^-$ as the dominant reactive species responsible for the degradation of TCs and ARGs. A Z-scheme heterojunction mechanism was proposed for the Bi_2WO_6/g-C_3N_4 composite to explain the enhanced charge separation. TC degradation primarily involved demethylation, deamidation, ring-opening, and oxidation reactions, and three possible degradation pathways were proposed. The reduction of ARGs was mainly attributed to the destruction of microbial cell structures and oxidative DNA damage induced by reactive species. Significant correlations were observed between ARGs and DOC, intI1, and 16S rRNA, indicating that DOC reduction plays an important role in controlling ARG proliferation. Notably, no significant ARG rebound was detected within three days after treatment. The Bi_2WO_6/g-C_3N_4 composite exhibited excellent photocatalytic oxidation performance for the simultaneous removal of TCs and ARGs, providing insights into the effective control of persistent organic contaminants.

Conflicts of interest

The authors declare that they have no known competing financial interests or personal relationships that could have appeared to influence the work reported in this paper.

Data availability

The authors confirm that the data supporting the findings of this study are available within the article and its supplementary information (SI). Supplementary information is available. See DOI: https://doi.org/10.1039/d5ra09524g.

Acknowledgements

This work was supported by Open Project of State Key Laboratory of Urban-rural Water Resources and Environment (Grant No. ES202419).

References

1 H. Su, H. Yin, R. Wang, Y. Wang, W. Orbell, Y. Peng and J. Li, Atomic-level coordination structures meet graphitic carbon nitride (g-C_3N_4) for photocatalysis: Energy conversion and environmental remediation, *Appl. Catal., B*, 2024, 123683, DOI: 10.1016/j.apcatb.2023.123683.

2 M. A. Khan, S. Mutahir, I. Shaheen, Y. Qunhui, M. Bououdina and M. Humayun, Recent advances over the doped g-C_3N_4 in photocatalysis: A review, *Coord. Chem. Rev.*, 2025, **522**, 216227, DOI: 10.1016/j.ccr.2024.216227.

3 B. Halling-Sørensen, S. Nors Nielsen, P. F. Lanzky, F. Ingerslev, H. C. Holten Lützhøft and S. E. Jørgensen, Occurrence, fate and effects of pharmaceutical substances in the environment- A review, *Chemosphere*, 1998, **36**, 357–393, DOI: 10.1016/S0045-6535(97)00354-8.

4 S. Li, C. Wang, Y. Liu, Y. Liu, M. Cai, W. Zhao and X. Duan, S-scheme MIL-101(Fe) octahedrons modified Bi_2WO_6 microspheres for photocatalytic decontamination of Cr(VI) and tetracycline hydrochloride: Synergistic insights,

reaction pathways, and toxicity analysis, *Chem. Eng. J.*, 2023, **455**, 140943, DOI: 10.1016/j.cej.2022.140943.

5 S. Wang, C. Li, H. Yin, B. Gao, Z. Yu, Y. Zhou, J. Wang, H. Xu, J. Wu and Y. Sun, A novel Ag/Bi/$Bi_2O_2CO_3$ photocatalyst effectively removes antibiotic-resistant bacteria and tetracycline from water under visible light irradiation, *Environ. Res.*, 2025, **264**, 120313, DOI: 10.1016/j.envres.2024.120313.

6 W. Xue, X. Shi, J. Guo, S. Wen, W. Lin, Q. He, Y. Gao, R. Wang and Y. Xu, Affecting factors and mechanism of removing antibiotics and antibiotic resistance genes by nano zero-valent iron (nZVI) and modified nZVI: A critical review, *Water Res.*, 2024, **253**, 121309, DOI: 10.1016/j.watres.2024.121309.

7 C. Sun, Q. Wang, J. D. Brubaker, P. M. Wright, C. D. Lerner, K. Noson, M. Charest, D. R. Siegel, Y. M. Wang and A. G. Myers, A robust platform for the synthesis of new tetracycline antibiotics, *J. Am. Chem. Soc.*, 2008, **130**, 17913–17927, DOI: 10.1021/ja806629e.

8 Y. Yuan, X. Zhu, Y. Liu, Z. An, H. Jia and J. Wang, Design of membrane-based microfluidic chip device based on bionic leaf and adsorption detection of tetracycline antibiotics by specific gel membrane, *Chem. Eng. J.*, 2024, **495**, 153394, DOI: 10.1016/j.cej.2024.153394.

9 X. Chen, Y. Yang, Y. Ke, C. Chen and S. Xie, A comprehensive review on biodegradation of tetracyclines: Current research progress and prospect, *Sci. Total Environ.*, 2022, **814**, 152852, DOI: 10.1016/j.scitotenv.2021.152852.

10 C. Zhou, C. Lai, D. Huang, G. Zeng, C. Zhang, M. Cheng, L. Hu, J. Wan, W. Xiong, M. Wen, X. Wen and L. Qin, Highly porous carbon nitride by supramolecular preassembly of monomers for photocatalytic removal of sulfamethazine under visible light driven, *Appl. Catal., B*, 2018, **220**, 202–210, DOI: 10.1016/j.apcatb.2017.08.055.

11 W. Shi, H. Zhang, J. Li, Y. Liu, R. Shi, H. Du and J. Chen, Occurrence and spatial variation of antibiotic resistance genes (ARGs) in the Hetao Irrigation District, China, *Environ. Pollut.*, 2019, **251**, 792–801, DOI: 10.1016/j.envpol.2019.04.119.

12 C. M. Manaia, J. Rocha, N. Scaccia, R. Marano, E. Radu, F. Biancullo, F. Cerqueira, G. Fortunato, I. C. Iakovides, I. Zammit, I. Kampouris, I. Vaz-Moreira and O. C. Nunes, Antibiotic resistance in wastewater treatment plants: Tackling the black box, *Environ. Int.*, 2018, **115**, 312–324, DOI: 10.1016/j.envint.2018.03.044.

13 L. Du, S. Ahmad, L. Liu, L. Wang and J. Tang, A review of antibiotics and antibiotic resistance genes (ARGs) adsorption by biochar and modified biochar in water, *Sci. Total Environ.*, 2023, **858**, 159815, DOI: 10.1016/j.scitotenv.2022.159815.

14 J. Fu, Y. Zhao, Q. Yao, O. Addo-Bankas, B. Ji, Y. Yuan, T. Wei and A. Esteve-Núñez, A review on antibiotics removal: Leveraging the combination of grey and green techniques, *Sci. Total Environ.*, 2022, **838**, 156427, DOI: 10.1016/j.scitotenv.2022.156427.

15 J. S. Cedeno-Munoz, S. A. Aransiola, K. V. Reddy, P. Ranjit, M. O. Victor-Ekwebelem, O. J. Oyedele, I. B. Perez-Almeida, N. R. Maddela and J. M. Rodriguez-Diaz, Antibiotic resistant bacteria and antibiotic resistance genes as contaminants of emerging concern: Occurrences, impacts, mitigations and future guidelines, *Sci. Total Environ.*, 2024, **952**, 175906, DOI: 10.1016/j.scitotenv.2024.175906.

16 M. N. Pham, F. Nishimura, J. C. W. Lan and K. S. Khoo, Recent advancement of eliminating antibiotic resistance bacteria and antibiotic resistance genes in livestock waste: A review, *Environ. Technol. Innovation*, 2024, **36**, 103751, DOI: 10.1016/j.eti.2024.103751.

17 M. G. Kotp and S.-W. Kuo, Harnessing solar energy with porous organic polymers: Advancements, challenges, economic, environmental impacts and future prospects in sustainable photocatalysis, *Mater. Today Chem.*, 2024, **41**, 102299, DOI: 10.1016/j.mtchem.2024.102299.

18 X. Yan, T. Zhang, S. Meng, P. Zhou, Y. Xu, Y. Wang and M. Xie, $BaFe_{12}O_{19}$/BiOBr S-scheme heterojunction magnetic nanosheets for high-efficiency photocatalytic degradation of 2-mercaptobenzothiazole, *Sep. Purif. Technol.*, 2023, 124746, DOI: 10.1016/j.seppur.2023.124746.

19 Y. Zha, X. He, Y. Wang, W. Chen, L. Chen, L. Chen, S. Wang, B. Yan, B. Ma and J. Li, Visible-light-response Fe-doped BiOCl microspheres with efficient photocatalysis-Fenton degradation of antibiotics, *J. Water Proc. Eng.*, 2024, **67**, 106225, DOI: 10.1016/j.jwpe.2024.106225.

20 Y. Sun, Y. Wu, D. Cai, D. Zou and Y. Li, Enhanced adsorption-photocatalysis synergy by S-scheme In-MOG/carbon doped ZnO for rapid chlortetracycline removal: Exploring synergistic mechanisms, environmental implications and continuous flow applications, *Sep. Purif. Technol.*, 2025, **354**, 129394, DOI: 10.1016/j.seppur.2024.129394.

21 W. Guo, T. Guo, Y. Zhang, L. Yin and Y. Dai, Progress on simultaneous photocatalytic degradation of pollutants and production of clean energy: A review, *Chemosphere*, 2023, **339**, 139486, DOI: 10.1016/j.chemosphere.2023.139486.

22 K. Xu, Z. Zhu, C. Hu, J. Zheng, H. Peng and B. Liu, Fabrication of unconventional S-scheme NiAl LDH/$Ag_6Si_2O_7$ heterojunction photocatalysts: outstanding photocatalytic performance and photocatalytic mechanism for tetracycline degradation, *Colloids Surf., A*, 2023, **674**, 131806, DOI: 10.1016/j.colsurfa.2023.131806.

23 L. Wang, H. Yang, Q. Wu and R. Ma, Construction of visible-light-response K, Na doped g-C_3N_4/FeOCl photocatalysis-self-Fenton system for pollutants degradation in water, *Int. J. Hydrogen Energy*, 2024, **80**, 495–506, DOI: 10.1016/j.ijhydene.2024.07.128.

24 N. Chaharlangi, P. Molaei and R. Yousefi, One-step fabrication of S-scheme ZnO/g-C_3N_4 composites for enhanced environmental photocatalysis, *J. Alloys Compd.*, 2024, 177289, DOI: 10.1016/j.jallcom.2024.177289.

25 J. Liu, Y. Gao, Z. Zhang, R. Dang, R. N. El Houda Tiri, M. Bekmezci, R. Bayat, R. Darabi and F. Sen, Photocatalytic activity of TiO_2-ZnO/g-C_3N_4 nanocomposites for methylene orange and Rhodamine B dyes removal from water and photocatalytic hydrogen generation,

Chemosphere, 2023, **339**, 139426, DOI: 10.1016/j.chemosphere.2023.139426.

26 J.-Y. Tang, C.-C. Er, X. Y. Kong, B.-J. Ng, Y.-H. Chew, L.-L. Tan, A. R. Mohamed and S.-P. Chai, Two-dimensional interface engineering of g-C_3N_4/g-C_3N_4 nanohybrid: Synergy between isotype and p–n heterojunctions for highly efficient photocatalytic CO2 reduction, *Chem. Eng. J.*, 2023, **466**, 143287, DOI: 10.1016/j.cej.2023.143287.

27 X. Zhang, A. Guo, Y. Zou, H. Liu, Y. Jiang, B. Qin, M. Liu and A. Cai, Coupled capture and photocatalysis of g-C_3N_4 based magnetic composites: Mechanism and disinfection activity against Staphylococcus aureus, *Mater. Sci. Semicond. Process.*, 2024, **179**, 108533, DOI: 10.1016/j.mssp.2024.108533.

28 S. Rauf, S. Mahmood, M. Javed, S. Mansoor, M. Umar, S. Shahid, S. Mansoor, A. Zidan, R. Nawaz, S. Iqbal, A.-E. Farouk, S. Aloufi, H. M. Abdelmigid and T. Akhter, Innovative S-Scheme heterojunctions: Boosting methylene blue degradation and antimicrobial efficacy with Ni–CoS@S-g-C_3N_4, *Opt. Mater.*, 2024, **157**, 116335, DOI: 10.1016/j.optmat.2024.116335.

29 F. K. Alharbi, A. E. A. E. Albadri, A. Modwi and S. M. Saleh, Effectiveness of Ag@NiO@g-CN photocatalysts: Green fabrication and superior photocatalysis capability, *Opt. Mater.*, 2024, **152**, 115410, DOI: 10.1016/j.optmat.2024.115410.

30 Y. Jia, X. Tong, H. Zhou, J. Zhang, Y. Chen, L. Zhang, Y. Yang and X. Ji, Construction of carbon-doped mesoporous g-C_3N_4 catalytic nanoreactor via bubble template method for visible-light photocatalysis, *J. Alloys Compd.*, 2024, **987**, 174217, DOI: 10.1016/j.jallcom.2024.174217.

31 C. V. Reddy, R. R. Kakarla, B. Cheolho, J. Shim and T. M. Aminabhavi, Heterostructured 2D/2D $ZnIn_2S_4$/g-C_3N_4 nanohybrids for photocatalytic degradation of antibiotic sulfamethoxazole and photoelectrochemical properties, *Environ. Res.*, 2023, **225**, 115585, DOI: 10.1016/j.envres.2023.115585.

32 J. Jia, Q. Zhang, K. Li, Y. Zhang, E. Liu and X. Li, Recent advances on g–C_3N_4–based Z-scheme photocatalysts: Structural design and photocatalytic applications, *Int. J. Hydrogen Energy*, 2023, **48**, 196–231, DOI: 10.1016/j.ijhydene.2022.09.272.

33 F. M. Cadan, C. Ribeiro and E. B. Azevedo, Improving g-C_3N_4:WO_3 Z-scheme photocatalytic performance under visible light by multivariate optimization of g-C_3N_4 synthesis, *Appl. Surf. Sci.*, 2021, **537**, 147904, DOI: 10.1016/j.apsusc.2020.147904.

34 Z. Chen, Y. Gao, F. Chen and H. Shi, Metallic NiSe cocatalyst decorated g-C_3N_4 with enhanced photocatalytic activity, *Chem. Eng. J.*, 2021, **413**, 127474, DOI: 10.1016/j.cej.2020.127474.

35 Y. Song, J. Qi, J. Tian, S. Gao and F. Cui, Construction of Ag/g-C_3N_4 photocatalysts with visible-light photocatalytic activity for sulfamethoxazole degradation, *Chem. Eng. J.*, 2018, **341**, 547–555, DOI: 10.1016/j.cej.2018.02.063.

36 S. Li, Y. Liu, Y. Xiao, H. Ma and J. Duan, Research progress, trends, and updates on pollutants removal by Bi_2WO_6-based photocatalysts under visible light irradiation, *Heliyon*, 2024, **10**, e27115, DOI: 10.1016/j.heliyon.2024.e27115.

37 Z. Yuan, H. Zhang, J. Jiang, H. Wang, X. Zhao, Z. Wang, Z. Jiang and H. He, Recent advances, modification strategies and perspectives of Bi_2WO_6 in photocatalytic CO_2 reduction reaction, *J. Environ. Sci.*, 2024, **156**, 157–172, DOI: 10.1016/j.jes.2024.09.007.

38 B. O. Orimolade, A. O. Idris, U. Feleni and B. Mamba, Recent advances in degradation of pharmaceuticals using Bi_2WO_6 mediated photocatalysis – A comprehensive review, *Environ. Pollut.*, 2021, **289**, 117891, DOI: 10.1016/j.envpol.2021.117891.

39 X. Liu, S. Gu, Y. Zhao, G. Zhou and W. Li, $BiVO_4$, Bi_2WO_6 and Bi_2MoO_6 photocatalysis: A brief review, *J. Mater. Sci. Technol.*, 2020, **56**, 45–68, DOI: 10.1016/j.jmst.2020.04.023.

40 L. Chen, B. Xu, M. Jin, L. Chen, G. Yi, B. Xing, Y. Zhang, Y. Wu and Z. Li, Excellent photocatalysis of Bi_2WO_6 structured with oxygen vacancies in degradation of tetracycline, *J. Mol. Struct.*, 2023, **1278**, 134911, DOI: 10.1016/j.molstruc.2023.134911.

41 F. Dong, C. Li, G. He, X. Chen and X. Mao, Kinetics and degradation pathway of sulfamethazine chlorination in pilot-scale water distribution systems, *Chem. Eng. J.*, 2017, **321**, 521–532, DOI: 10.1016/j.cej.2017.03.130.

42 Y. Zhu, Y. Wang, Q. Ling and Y. Zhu, Enhancement of full-spectrum photocatalytic activity over $BiPO_4$/Bi_2WO_6 composites, *Appl. Catal., B*, 2017, **200**, 222–229, DOI: 10.1016/j.apcatb.2016.07.002.

43 B. Chong, L. Chen, W. Wang, D. Han, L. Wang, L. Feng, Q. Li and C. Li, Visible-light-driven Ag-decorated g-C_3N_4/Bi_2WO_6 Z-scheme composite for high photocatalytic activity, *Mater. Lett.*, 2017, **204**, 149–153, DOI: 10.1016/j.matlet.2017.06.033.

44 Z. Ren, F. Chen, K. Wen and J. Lu, Enhanced photocatalytic activity for tetracyclines degradation with Ag modified g-C_3N_4 composite under visible light, *J. Photochem. Photobiol., A*, 2020, **389**, 112217, DOI: 10.1016/j.jphotochem.2019.112217.

45 P. Niu, L. Zhang, G. Liu and H. M. Cheng, Graphene-Like Carbon Nitride Nanosheets for Improved Photocatalytic Activities, *Adv. Funct. Mater.*, 2012, **22**, 4763–4770, DOI: 10.1002/adfm.201200922.

46 J. Li, H. Hao and Z. Zhu, Construction of g-C_3N_4-WO_3-Bi_2WO_6 double Z-scheme system with enhanced photoelectrochemical performance, *Mater. Lett.*, 2016, **168**, 180–183, DOI: 10.1016/j.matlet.2016.01.058.

47 Y. Tan, Z. Shu, J. Zhou, T. Li, W. Wang and Z. Zhao, One-step synthesis of nanostructured g-C_3N_4/TiO_2 composite for highly enhanced visible-light photocatalytic H_2 evolution, *Appl. Catal., B*, 2018, **230**, 260–268, DOI: 10.1016/j.apcatb.2018.02.056.

48 X. Miao, X. Shen, J. Wu, Z. Ji, J. Wang, L. Kong, M. Liu and C. Song, Fabrication of an all solid Z-scheme photocatalyst g-C_3N_4/GO/AgBr with enhanced visible light photocatalytic activity, *Appl. Catal., A*, 2017, **539**, 104–113, DOI: 10.1016/j.apcata.2017.04.009.

49 S. Ji, Y. Yang, Z. Zhou, X. Li and Y. Liu, Photocatalysis-Fenton of Fe-doped g-C_3N_4 catalyst and its excellent degradation

performance towards RhB, *J. Water Proc. Eng.*, 2021, **40**, 101804, DOI: 10.1016/j.jwpe.2020.101804.

50 C. Liu, K. Wu, G. Meng, J. Wu, B. Peng, J. Hou, Z. Liu and X. Guo, Explore the properties and photocatalytic performance of iron-doped g-C3N4 nanosheets decorated with Ni_2P, *Mol. Catal.*, 2017, **437**, 80–88, DOI: 10.1016/j.mcat.2017.02.038.

51 J. Ren, W. Wang, S. Sun, L. Zhang and J. Chang, Enhanced photocatalytic activity of Bi_2WO_6 loaded with Ag nanoparticles under visible light irradiation, *Appl. Catal., B*, 2009, **92**, 50–55, DOI: 10.1016/j.apcatb.2009.07.022.

52 A. Verma, S. Kumar and Y.-P. Fu, A ternary-hybrid as efficiently photocatalytic antibiotic degradation and electrochemical pollutant detection, *Chem. Eng. J.*, 2021, **408**, 127290, DOI: 10.1016/j.cej.2020.127290.

53 Y. Zhou, Y. Zhang, M. Lin, J. Long, Z. Zhang, H. Lin, J. C. Wu and X. Wang, Monolayered Bi2WO6 nanosheets mimicking heterojunction interface with open surfaces for photocatalysis, *Nat. Commun.*, 2015, **6**, 8340, DOI: 10.1038/ncomms9340.

54 Y. Gan, K. Zhu, W. Xia, S. Zhu, Z. Tong, W. Chen, Y. Wang and B. Lin, Strongly coupled Fe/N co-doped graphitic carbon nanosheets/carbon nanotubes for rapid degradation of organic pollutants via peroxymonosulfate activation: Performance, mechanism and degradation pathways, *Sep. Purif. Technol.*, 2022, **302**, 122113, DOI: 10.1016/j.seppur.2022.122113.

55 I. T. Bujak, M. Pocrnić, K. Blažek, K. Bojanić, P. Trebše, A. T. Lebedev and N. Galić, Radiation-induced degradation of doxazosin: Role of reactive species, toxicity, mineralization and degradation pathways, *J. Water Proc. Eng.*, 2023, **51**, 103401, DOI: 10.1016/j.jwpe.2022.103401.

56 M. Pelaez, A. A. de la Cruz, K. O'Shea, P. Falaras and D. D. Dionysiou, Effects of water parameters on the degradation of microcystin-LR under visible light-activated TiO_2 photocatalyst, *Water Res.*, 2011, **45**, 3787–3796, DOI: 10.1016/j.watres.2011.04.036.

57 D. Xia and I. M. C. Lo, Synthesis of magnetically separable Bi_2O_4/Fe_3O_4 hybrid nanocomposites with enhanced photocatalytic removal of ibuprofen under visible light irradiation, *Water Res.*, 2016, **100**, 393–404, DOI: 10.1016/j.watres.2016.05.026.

58 D. N. Kessler, V. K. Fokuhl, M. S. Petri and A. Spielmeyer, Abiotic transformation products of tetracycline and chlortetracycline in salt solutions and manure, *Chemosphere*, 2019, **224**, 487–493, DOI: 10.1016/j.chemosphere.2019.02.169.

59 S. Wang, Z. Zhou, R. Zhou, Z. Fang and P. J. Cullen, Highly synergistic effect for tetracycline degradation by coupling a transient spark gas–liquid discharge with TiO_2 photocatalysis, *Chem. Eng. J.*, 2022, **450**, 138409, DOI: 10.1016/j.cej.2022.138409.

60 W. H. Gaze, L. Zhang, N. A. Abdouslam, P. M. Hawkey, L. Calvo-Bado, J. Royle, H. Brown, S. Davis, P. Kay, A. B. Boxall and E. M. Wellington, Impacts of anthropogenic activity on the ecology of class 1 integrons and integron-associated genes in the environment, *ISME J.*, 2011, **5**, 1253–1261, DOI: 10.1038/ismej.2011.15.

61 M. V. Riquelme Breazeal, J. T. Novak, P. J. Vikesland and A. Pruden, Effect of wastewater colloids on membrane removal of antibiotic resistance genes, *Water Res.*, 2013, **47**, 130–140, DOI: 10.1016/j.watres.2012.09.044.